Effects of Elevated Intracranial Pressure on a Cerebral Vein Model

Nathaniel Davis

Thesis submitted to the faculty of the
Virginia Polytechnic Institute and State University
in partial fulfillment of the requirements for the degree of

Master of Science
in

Biomedical Engineering

Anne Staples, Chair
John Robertson
Pamela VandeVord

August 8, 2024
Blacksburg VA

Keywords: Brain Injury, Computational Fluid-Solid Dynamics, Intracranial Pressure, Cerebral Vasculature

Effects of Elevated Intracranial Pressure on a Cerebral Vein Model

Nathaniel Davis

Abstract

Nonfatal strangulation (NFS) can cause severe physical and psychological injury. Instances of NFS are correlated with a heightened risk of lethal violence between partners [1]. While NFS does not result in death, it can result in severe hypoxic brain injury (HBI) and has been shown to increase the likelihood of an eventual fatality in the relationship eightfold [1]. Unfortunately, minimal quantitative biomechanical research has been performed to study strangulation injury, and detection and diagnosis of NFS, which often relies upon visible injuries, remains challenging [2]. The effects of occluded cerebral venous flow on intracranial pressure (ICP) have not been considered in a model for HBI as opposed to the context of stroke and neonatal hypoxic-ischemic encephalopathy.

In this project, the effects of elevated ICP on the hemodynamics and structural dynamics of a diploic vein were considered. This was done by performing transient coupled fluid-structure simulations on a segment of an intracranial vein that sought to replicate the ICP surge experienced during strangulation. The vessel model was created by isolating a segment of an intracranial vessel. Using the software 3D Slicer, the skull was extracted and exported as an STL file. From there, a segment of a diploic vein was isolated and edited by importing the STL into Blender. The segment was then processed using MeshLab and Blender to make it a solid geometry and remove potential complications.

Once the vessel segment was isolated and processed, it was exported as an STL file into a commercial solver from ANSYS, Inc., Canonsburg, PA, USA. Using a coupling system of the Ansys Fluent and Mechanical models, a transient Fluid-Solid Interaction (FSI) simulation was performed by coupling ANSYS' Fluent and Mechanical models. In the simulation, blood flowed steadily through the vessel, and the data for FSI was recorded. The software was used to simulate the deformation and stress of the blood vessels caused by the blood flow for elevated intracranial pressure events for five different durations and magnitudes.

Following the FSI simulations, the total deformation, equivalent stress, dynamic pressure, static pressure, and fluid velocity were plotted. The results show that altering the pressure duration can increase average total vessel wall deformation by up to 356.35%, average equivalent stress by 331.11%, dynamic pressure by 19.28%, and decrease static pressure by 30.94%. Likewise, increasing the magnitude of pressure can also increase the dynamic pressure by 17.17 %, the maximum velocity by 16.77%, and can decrease the static pressure by 27.31%. The statistical behavior of each type of modification was unique, as altering the duration created a logarithmic plot while changing the magnitude of pressure created a second power plot. With the provided data, researchers will better understand the effects of NFS-like elevated intracranial pressure on cerebral vasculature.

Effects of Elevated Intracranial Pressure on a Cerebral Vein Model

Nathaniel Davis

General Audience Abstract

Nonfatal strangulation (NFS) has been identified as a leading indicator of escalating partner violence. The first occurrence of NFS in an intimate partnership correlated with an 8-fold increase in the risk of future attacks that are fatal by that partner. While NFS does not result in the immediate death of the victim, it can still cause severe physical and psychological harm. This includes traumatic brain injury from lack of proper blood flow, increased intracranial pressure (ICP), and hypoxia. Quantitative research on strangulation injury has mainly been carried out by forensics researchers, resulting in a lack of understanding of the biomechanics of nonfatal strangulation. This lack of knowledge, coupled with the frequent absence of visible injuries in victims of NFS, makes diagnosing NFS events particularly difficult. This study aims to begin to fill this gap by developing a computational biomechanics model of a phenomenon that occurs during NFS. The model examines how altering the duration and magnitude of a pressure wave that mimics the increased intracranial pressure during NFS can impact the blood flow and vessel motions in an intracranial blood vessel. The blood vessel model was extracted from a computed tomography (CT) scan of a patient's skull, preprocessed, and transferred into ANSYS finite element modeling software. Fluid-solid interaction (FSI) simulations were performed in ANSYS, which allowed the study of blood pressure, blood velocity, vessel deformation, and vessel stress. The results showed that increasing either the magnitude or duration of the pressure wave caused an increase in vessel stress and deformation. The results also showed that doing either increased the maximum blood velocity and dynamic pressure while decreasing the static pressure of the blood. These results contribute toward the understanding of the biomechanics of nonfatal strangulation. The model developed in this project may serve as the foundation for more complex models in future studies.

Acknowledgments

I wish to dedicate this page to all those who have helped me in the research and creation of this thesis. First, I would like to thank my advisor and committee chair, Dr Anne Staples. I thank her for all the academic and emotional support she has provided me while working towards my master's degree. I would also like to extend my gratitude towards Mrigank Dhingra for his help in developing the computational model on ANSYS 2024: Student Edition Software. I would not have been able to complete this thesis without either of them. I would also like to thank Dr. VandeVord and Dr. Robertson for serving on my committee. I am grateful for their patience and commitment in helping me complete my thesis and master's degree.

I would also like to extend my sincerest gratitude to Kelsey Wall and all faculty and administration in the Biomedical Engineering and Mechanics department at Virginia Tech. Thanks to their patience and guidance throughout my academic journey, I completed my thesis and fulfilled my graduation requirements on time.

I would also like to thank my family for their love and support, especially as a graduate student. I would not be the student or man I am today without their emotional support and belief in my potential as a scholar. I am genuinely grateful to have such a supportive family.

Table of Contents

List of Figures

List of Tables

List of Abbreviations

Abbreviation	Meaning
CSF	Cerebrospinal Fluid
CT	Computed Tomography
DV	Diploic Vessel
ES	Equivalent Stress
FSI	Fluid-Solid Interface
ICP	Intracranial Pressure
IPV	Intimate Partner Violence
NFS	Non-Fatal Strangulation
NSE	Navier Stokes Equation
TD	Total Deformation

Introduction

Background

Incidents of non-fatal strangulations (NFS) between intimate partners can increase the probability of homicide by a factor of more than 7 [3]. Likewise, NFS has been reported in 10% of abuse cases and 45% of attempted homicide cases between intimate partners [3]. To make matters worse, detecting NFS in victims has remained a difficult task. Even in fatal strangulation instances, 40% of the victims show no external sign of strangulation [2]. However, internal and chronic injuries and complications can occur, such as damage to the carotid artery and jugular veins [2]. There is also the matter of the psychological and neurological damage NFS brings to the victim. NFS victims have been reported to develop clinically significant signs of Post-Traumatic Stress Disorder (PTSD), hyperarousal, dissociation, and avoidance [4]. Likewise, deprivation of oxygenated blood to the brain at repetitive intervals can cause long-term neurovascular changes and impair cognitive abilities [4]. Because of these factors, NFS has remained an understudied form of intimate partner violence (IPV). Likewise, NFS can result in hypoxic brain injury as blocking the jugular and carotid can prevent oxygenated blood from flowing properly [4]. Additionally, blood pressure-related injuries such as aneurysms and stroke can also be a consequence of NFS [4].

Research Plans and Goals

This study aims to develop a first computational model for the effects of simulated nonfatal strangulation intracranial pressure conditions on the hemodynamics and wall deformation in a cerebral blood vessel. The study considers the effects of elevated intracranial pressure on the hemodynamics and vessel wall structural dynamics of a diploic vein. This is done by performing transient coupled fluid-structure simulations on a segment of the vein to represent the elevated intracranial pressure (ICP) experienced during an NFS event to determine the effects of the surge in ICP on the stress and deformation of the vessel. The effects of the duration and magnitude of the elevated ICP event on the vessel wall and hemodynamics were investigated. Future iterations of this model will include more extensive parts of the cerebrovascular network and coupled representations of the pressures in the different intracranial compartments. These modeling efforts aim to develop a mechanistic understanding of the biomechanics of strangulation that may enable new detection and diagnosis methods.

Literature Review

Strangulation and Injuries

The brain is a vast network of neurological tissue and complex vasculature, with the neck being the literal chokepoint of all of it. Likewise, the neck is a highly vulnerable point in human anatomy where any significant pressure and obstruction can cause severe damage to the brain. Like regular strangulation, NFS involves the obstruction of airflow and blood flow in the neck of the victim via external pressure [3]. Unlike conventional strangulation, the assailant ceases the pressure before the victim dies. Despite the lack of lethality, NFS can lead to serious health complications and could potentially lead to a cascade of effects within the intracranial vasculature in addition to psychological trauma. It is essential to divide the types of injury into three categories. The first category can be described as physical. This includes contusions and marks on the neck from the assailant's hand. The second category can be defined as neurological. This includes intracranial abnormalities and trauma caused by the event. There is also the psychological aspect of NFS, the second category, such as PTSD and other psychological complications caused by intense trauma. The primary consequence of strangulation is hypoxia, which can have various adverse effects on human neurology. There are also many other physiological effects of strangulation and the hypoxia that follow.

Physical injuries are more visible and, thus, are easier to detect and account for as the physician can notice them and have the most distinctive symptoms. The most common form of injury for NFS comes in the form of sore throats, as they are reported in 60% to 70% of strangulation cases [5]. Additionally, contusions around the neck and throat are notable forms of physical injury [4]. While there are multiple injuries that a victim can incur during NFS, most external signs are not present or lasting following the incident.

There is also the psychological toll that NFS takes on the victim. In studies involving the direct question of female victims, 83% of them reported at least psychiatric symptom up to 2 weeks following the event [6]. Likewise, victims of NFS have been known to develop clinically significant PTSD symptoms [4]. Victims may also experience cognitive side effects following NFS and are consistent with post-concussive symptoms, such as headaches, vision problems, and disturbances in mood and sleep [4]. The effect of NFS cannot be understated and can have a devastating impact on the victims' well-being and safety.

Many injuries caused by NFS go beyond damage to the neck, such as the vasculature of the brain, as many survivors of strangulation generally demonstrate a variety of neurological disabilities such as agitation, Korsakoff's syndrome, and even dementia [7]. Hypoxic and anoxic brain injuries are expected consequences of NFS, as the brain receives an insufficient amount of oxygen during strangulation [4]. Strangulation causes an increase in intracranial pressure as constriction of the neck leads to a significant increase in pressure within the skull [8]. Additionally, strangulation can lead to other neurovascular injuries following the event, such as stroke, aneurysm, and other blood pressure-related injuries [9]. Other possible sequelae can manifest even after a significant amount of time has passed after NFS. Delayed anoxic encephalopathy is brain damage that becomes present days or weeks after an instance of NFS and can cause blindness, dystonia, choreoathetosis, and much more [2]. It cannot be understated that NFS yields cripple severe injuries, despite the lack of lethality in the form of assault.

Intimate Partner Violence and Detection of Non-fatal strangulation

NFS is a dangerous indicator of IPV and can lead to more severe forms of violence from the assailant. It is crucial to note that NFS rarely occurs in isolated incidents. More instances of NFS usually accompany them and can be viewed as an ongoing method of control through coercion from the assailant [4]. Additionally, cases of women being murdered by their intimate partner have often been preceded by NFS. In a study by Glass et al., approximately 43% of homicide cases against women by their intimate partner had experienced some form of NFS [6]. Likewise, 45% of attempted homicide cases experienced NFS [6].

The most sinister aspect of NFS is the lack of evidence it leaves behind. Within both the forensic and medical circles, the detection of strangulation has overall remained a problematic task. Survivors of NFS are often misdiagnosis and under-diagnosis by medical professionals [4]. This is most likely due to the broad symptoms associated with NFS and the inconsistency of symptoms that do appear. The signs of NFS currently remain poorly defined as it leaves very few observable injuries [6]. Most physical injuries occur around the neck and damage its vasculature, but most clinicians continue to have a hard time identifying them. Even in fatal strangulation, 40% of victims have physical signs of strangulation. NFS survivors are no better, as a landmark study in Los Angeles from 2001 showed that only 50% of NFS victims showed any visible injury [4].

Even within law and forensics, NFS remains a novel and underestimated issue. Due to most forensics research prioritizing deadly forms of assault, examining the evidence of NFS remains an understudied field in published literature [10]. There is also the matter of the legal identification of NFS. Since NFS leaves very minute injuries, if any, law enforcement remains under-trained in identifying NFS [10]. Likewise, NFS leaves injuries too obscured to be photographed to be used as evidence in a court case [9]. This can be a crucial detail as 911 dispatchers are the first, and sometimes only, line of contact between the public and the victim [10].

Infinite Element Model of Cerebral Vasculature and Blood Properties

Although NFS remains understudied, the intracranial vasculature is well modeled. While the specific effects of NFS on intracranial vasculature have remained understudied, many researchers have developed models and simulations based on the symptoms and adverse effects, such as ischemia. A research paper by Bing et al. has developed a Finite Element Model for the cerebrovascular system [11]. The study involved giving the intracranial cerebral artery a wall thickness of 0.1 mm and utilizing the Ogden model for the simulation. The researchers also provided properties to cerebral tissue around the intracranial arteries should this research extend to integrating this model into a cerebral analog.

The properties of blood itself also have an extensive background in modeling. While most contemporaries view blood as a non-Newtonian fluid, some microfluidic research views it as a

Newtonian fluid. An experiment by Jain et al. performs a simplified Computational Fluid Dynamics (CFD). This simulation treats whole blood as a Newtonian fluid with density and viscosity, similar to the CFD simulation of this study [12]. The experiment intended to study intracranial aneurysms, providing an excellent precedent for our CFD. However, the direction of blood flow can be difficult, especially in an intricate part like the skull. The brain needs an ample, constant blood supply and a complex irrigation system for the cerebrospinal fluid (CSF). This can cause the direction of blood flow for certain vessels to be less than intuitive.

Current methods are implemented in this research. For example, the ANSYS software successfully simulates vascular research. The study by Jain et al. utilized the FSI ANSYS software for their research. Likewise, research by Li et al. performed an ANSYS FSI simulation for abdominal aortic aneurysms [13]. Likewise, the ANSYS FSI simulation had a 10% error from experimental data. This proved to be very useful in validating the use of ANSYS in our own FSI model.

Methods

Model

Extraction

This research involved extracting a model from preexisting DICOM data and converting it into a useful model. Afterward, the extracted blood vessels were processed in Blender to facilitate simulations. Finally, the processed extraction was imported into the ANSYS Software. A transient Fluid-Solid Interaction (FSI) simulation was performed on the ANSYS Software.

Extracting the vessel from scan data was the first step in developing the model. The vessel was extracted from DICOM data provided by an Embodi3D tutorial [14]. According to the metadata in the files, the DICOM data was a CT scan of a female from 2008. The CT scan was processed using the open-access 3D Slicer program with a detection tolerance of 1400. This allowed the program to select the more complex, osseous material to generate the skull based on the contrast within the DICOM files. A layer from the sagittal plane and the 3D model generated from this technique can be seen in **Figure 1**. There were empty sections of the skull due to the contrast between voxels. This was due to the contrast of the rigid and soft tissue. Given the shape and contrast, one could assume this structure was a vessel. After determining this was a vessel of some sort, it was soon determined to be a diploic vessel. These are vessels that exist in the cranial dipole within the plate of the skull itself [15]. Upon closer examination, these diploic vessel were determined to be a 'Serpentine-Type' DV [16] . This assumption was made on the fact that the vessel was in the parietal segment of the bone and its long, riverlike appearance [16], [17].

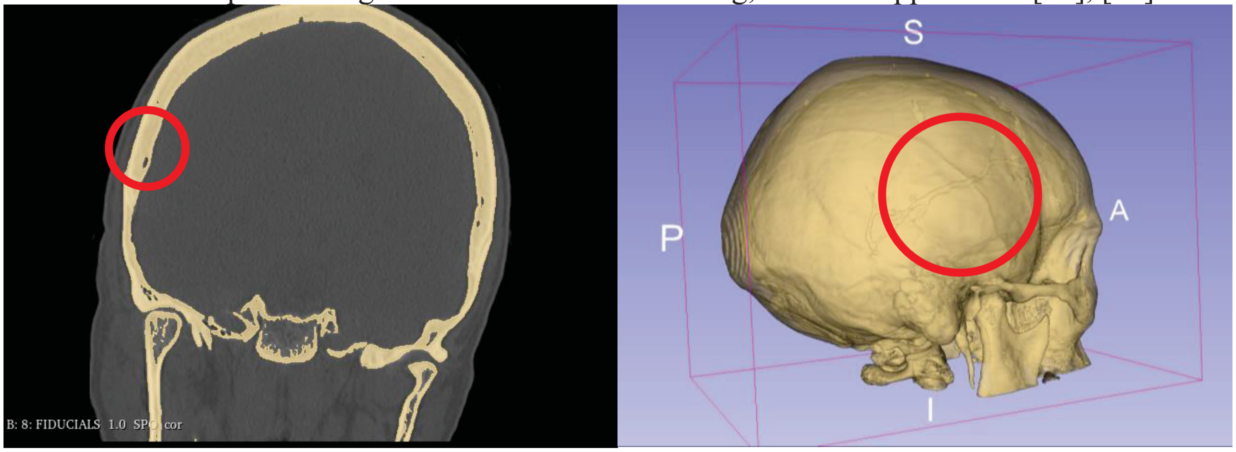

Figure 1: Sagittal view of patient's skull (left) from the DICOM CT data and extracted skull from 3D Slicer software.

Preprocessing

The next step was the extraction of the vessel from the skull itself. As seen in **Figure 1**, the vein was located within the skull. After extracting the skull, the vessel was isolated and processed on Blender. The imported skull was preprocessed to remove the unnecessary geometry and isolate the targeted vessel portion. The isolated vessel relative transferred into ANSYS can be seen in **Figure 2**. Once the vessel was isolated, it was given a wall thickness of 0.10 mm to match preexisting intracranial models [11]. The thickness would extend outward as it was assumed the DICOM data was detecting the vessel's lumen. The vessel's location within the skull can be seen in **Figure 4**. The mesh data for the isolated vessel can also be found in **Table 1**. It is important to note that the original vessel segment had significantly more vertices but was reduced by the decimation feature in Blender to facilitate computation.

Table 1: Vessel Model Properties.

Vessel Mesh Properties	
Number of elements	50096
Number of nodes	25028
Number of External Faces	1472

Following the preprocessing of the targeted vessel, the file was converted to an STL and imported into the simulation software. This study utilized the ANSYS software as it had an extensive toolbox for modeling and simulating Fluid-Structure Interactions (FSI). The program achieved this by having multiple analysis systems for different types of simulations. In this case, two components were used. The first was the Transient Structural Analysis System. Here, the vessel was converted to a solid and given mesh and material properties. The second component is the Fluid Flow (Fluent) Analysis System. A fluid volume was generated using the preexisting vessel as a template. The volume was given material properties and a flow profile. The vessel was given hyper-elastic material based on 2nd-order Ogden elasticity in the ANSYS software. The vessel was filled with blood, and an FSI simulation was performed. The fluid volume used in ANSYS can be found in **Figure 3.**

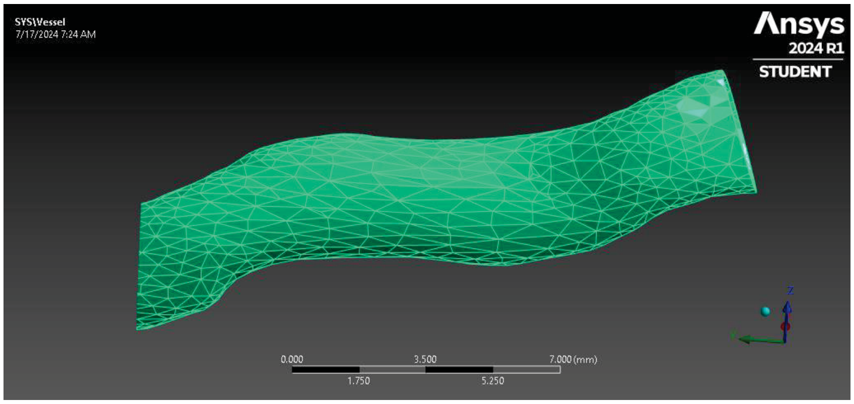

Figure 2: The vessel was imported as a solid transient structure in the ANSYS Workbench.

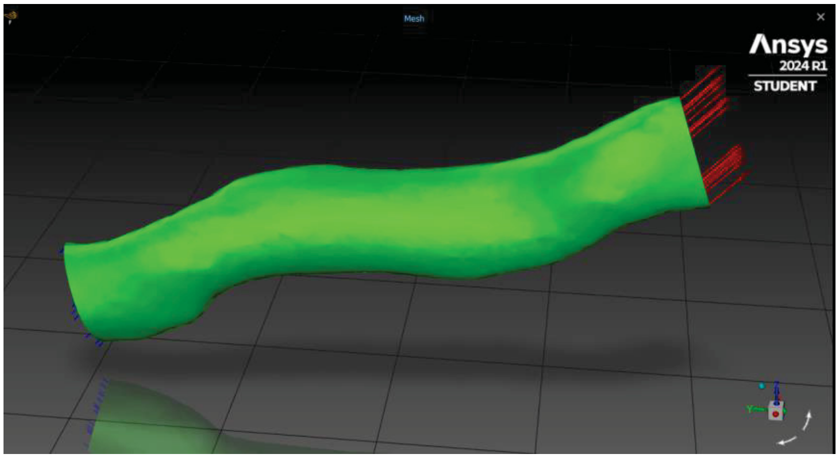

Figure 3: Fluid Flow (Fluent) mesh. Streamlines at vessel outlet plane

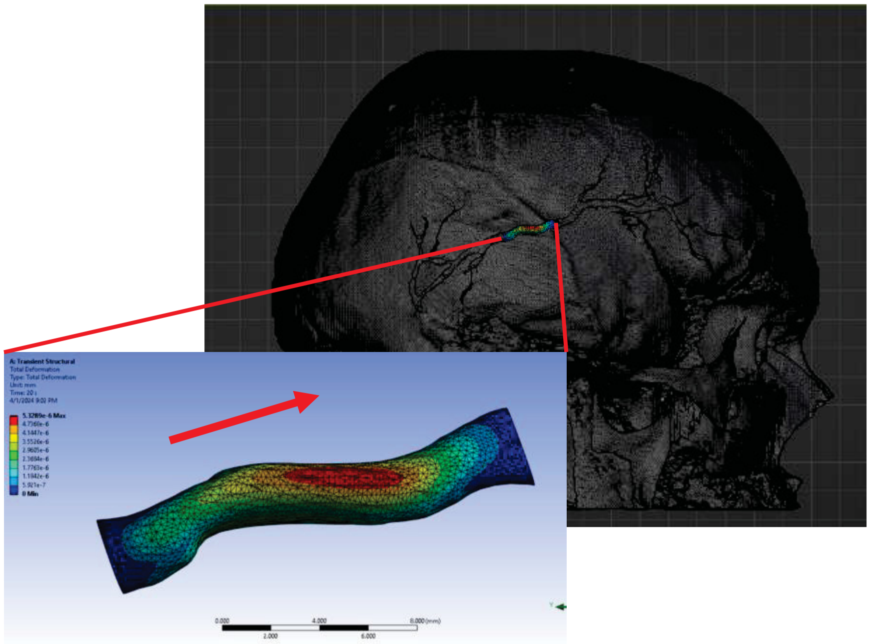

Figure 4: Extracted vessel in ANSYS superimposed onto skull model in Blender

Simulation

Vessel Properties and Material

The first part of the transient FSI ANSYS simulation was defining and modeling the transient solid component. Upon closely examining the vessel and its location within the parietal of the skull, it was identified as a diploic vessel. Unfortunately, diploic veins within humans have remained challenging to study due to their location within the dipole and have been inconsistently identified with most biomedical imaging [18]. Nevertheless, the extracted vessel segment was declared a diploic vein with blood flowing from the posterior to the anterior of the skull. This assumption was based on the assumption that the blood and fluid within the diploic veins within the parietal plate of the skull flow toward the sphenoparietal sinus through the pterion of the skull [18]. The sphenoparietal sinus is located in the anterior of the skull; thus, the flow of blood is posterior to the anterior [19].

The vessel extracted from the DICOM data needed to become a solid, usable body before performing any simulation and have a specific wall thickness. This was accomplished in Blender. After the extracted vessel geometry was given a 0.10 mm wall thickness throughout its entire length using the Solidify Modifier on Blender. The designated wall thickness was based on Bing et al.'s simulation [11]. While research by Bing et al. primarily focused on intracranial arteries, the difference in wall thickness should be negligible. It is also important to note that the vessel had a lumen that was more elliptical than circular. The minimum and maximum diameters were recorded in **Table 2** with the vessel's overall length. Likewise, the entire modeled vessel's length was recorded as 19.27 mm from end to end. The reason for selecting this portion of the intracranial vessel was because it was the longest portion of the extracted vessels that did not bifurcate or have holes in it. This model results from the Solidification and Decimation of the extracted DICOM mesh to an appropriate number of elements.

The material of the vessel also required a complicated approach. Due to the elastic properties of biological vessels, the 2nd Ogden Model for elasticity was used. This was based on the fact that the Ogden model has emerged for biological materials for theoretical and computational models [20]. Likewise, Paz et al. developed a transient FSI model on the ANSYS software that used the Ogden model to make the vessel elastic [21]. The strain energy density function for the Ogden is given by **Equation 1** [22]. It is important to note that no data on the anisotropy of the vessel wall can be used in this model [11]. As such, we had to develop the Ogden Model based on an idealized hyperelastic material based on data provided by Ansys. The program offered tabulated data for a hyperplastic Ogden model, including the shear and strain in the uniaxial, biaxial, and shear directions [23]. The data can be found in the **Appendix**. The material parameters (μ and α) can be found in **Table 3**. $\lambda 1$, $\lambda 2$, and $\lambda 3$ represent the three principal stretches: uniaxial, biaxial, and shear. However, Paz et al. simulated a 3rd-order Ogden model (N=3), while our simulation was conducted under the 2nd-order. This was due to the data provided by the ANSYS Ogden model tutorial. With this data, the best-fit curve was a 2nd-order Ogden model with no change in residuals between the 2nd and 3rd-order Ogden models. The 2nd Order Ogden model was used in all the simulations. The density of the vessel was also assumed to be 1100 kg/m^3 based on research by Hodis et al. [24]. This was the density value used for pulsatile simulation, so this model can easily be used in arterial blood flow. Overall, the model was assumed to be like a vein rather than an artery. This was because all NFS cases involve occlusion of venous blood flow. The least amount of strangulation pressure results in occlusion in venous blood flow out of the head, while more pressure results in occlusion of arterial blood to the brain.

$$\psi = \sum_{i=1}^{N} \frac{\mu_i}{\alpha_i} \cdot \left(\overline{\lambda_1}^{\alpha_i} + \overline{\lambda_2}^{\alpha_i} + \overline{\lambda_3}^{\alpha_i} - 3\right) \quad (1)$$

Table 2: Physical Vessel Properties

Vessel Property	**Value**
Minimum Diameter (mm)	01.37
Maximum Diameter (mm)	03.16
Length (mm)	19.27
Wall thickness (mm)	0.1
Density (kg/m^3)	1100

Table 3: Parameter for Ogden Model (N=2)

Ogden Values	
μ_1 (MPa)	2.5646E-07
α_1	27.976
μ_2 (MPa)	2.829
α_2	0.85415

Blood Properties and Flow

The second part of the transient FSI simulation in ANSYS was developing blood's material and flow properties. As stated previously, the blood flow in the vessel travels from the posterior of the skull to the anterior. The inlet boundary condition of the induced fluid was defined as a steady, laminar with a parabolic profile, adhering to the Law of Poiseuille [25]. Using a user-defined velocity profile based on Poiseuille's Formula in **Equation 2**. The velocity was given a parabolic velocity profile based on its maximum velocity calculated center within the lumen. The code for the user-defined function can be found in **Appendix C**.

$$U(r) = U_{max}(1 - \frac{r^2}{R^2}) \quad \mathbf{(2)}$$

For the simulation, blood was modeled as Newtonian liquid water found as a preset in ANSYS. As stated earlier, other studies have modeled blood as a Newtonian liquid for simplicity. However, the density and dynamic viscosity of the liquid were altered to be more like whole blood. In this case, whole blood has a constant density of 1060 kg/m^3 and a constant viscosity of 3.5 cP (.0035 Pa•s) [26]. **Table 4** shows the properties of the blood used in the fluid portion of the ANSYS FSI simulation**.**

Table 5: Physical Blood Properties

Whole Blood Property	Value
Density	1060 kg/m^3
Viscosity	0.0035 Pa

ANSYS Fluent measures and determines fluid flow properties using the Navier-Stokes equation (NSE). The software discretizes the NSE using the finite volume method [12]. This involves dividing the domain of the simulation into a series of small, interconnected, cell-like control volumes. The key values are measured at the centroid of these volumes [27]. The Navier-Stoke equations used for this simulation can be found in Cartesian form in **Equations 3.1** to **3.3** as well as the Continuity **Equation in 3.4** [26]**.** These equations are used based on the assumption that the blood in this simulation has a laminar flow and is noncompressible and Newtonian. As such, there is no change in pressure or turbulence. The flow also operates in an environment without gravity.

$$\rho g_x - \frac{\partial p}{\partial x} + \mu\left(\frac{\partial^2 u}{\partial x^2} + \frac{\partial^2 u}{\partial y^2} + \frac{\partial^2 u}{\partial z^2}\right) = \rho\left(\frac{\partial u}{\partial t} + u\frac{\partial u}{\partial x} + v\frac{\partial u}{\partial y} + w\frac{\partial u}{\partial z}\right) \quad \textbf{(3.1)}$$

$$\rho g_y - \frac{\partial p}{\partial y} + \mu\left(\frac{\partial^2 v}{\partial x^2} + \frac{\partial^2 v}{\partial y^2} + \frac{\partial^2 v}{\partial z^2}\right) = \rho\left(\frac{\partial v}{\partial t} + u\frac{\partial v}{\partial x} + v\frac{\partial v}{\partial y} + w\frac{\partial v}{\partial z}\right) \quad \textbf{(3.2)}$$

$$\rho g_z - \frac{\partial p}{\partial z} + \mu\left(\frac{\partial^2 w}{\partial x^2} + \frac{\partial^2 w}{\partial y^2} + \frac{\partial^2 w}{\partial z^2}\right) = \rho\left(\frac{\partial w}{\partial t} + u\frac{\partial w}{\partial x} + v\frac{\partial w}{\partial y} + w\frac{\partial w}{\partial z}\right) \quad \textbf{(3.3)}$$

$$\frac{\partial u}{\partial x} + \frac{\partial v}{\partial y} + \frac{\partial w}{\partial z} = 0 \quad \textbf{(3.4)}$$

Pressure Simulation

Since NFS has been known to cause TBI-like hypoxic brain injury. As such, it can cause an increase in intracranial pressure [8]. This increase in intracranial pressure can be modeled as a distinctive pressure wave. The pressure itself was based on the traumatic brain injury simulation performed by Neuberger et al. [28]. It is important to note that the initial and resting pressure of the intracranial spinal fluid is 20 mmHg standing up, which equates to 2.666E-3 MPa [29].

Before enacting a pressure wave onto the vessel, it must be extracted from a previously existing research paper. Neuberger et al. studied concussive injury using the fluid percussion injury (FPI) model. A voice-coil-drive FCI (VC-FCI) device wave was developed to allow researchers to apply a specific pressure wave of varying length and magnitude. This allowed them to study the effect of traumatic brain injury based on different types of fluctuations in fluid pressures. The graph of the other pressures studied can be found in **Figure 5**. The VC-FPI standard Waveform was used for simulations. This was because the waveform served as the baseline for their research. It is important to note that a machine delivered these pressure values to simulate TBI, not the values associated with TBI.

After the pressure was imported from Neuberger's research, it was stretched by a specific factor to last a set amount of time. Each trial was 30 seconds long, each comprising a different pressure length. Likewise, all trials have an initial grace period of 5 seconds for the FSI simulation to settle and reach a proper initial condition. After the 5-second mark, each trial endured a different pressure wave. While the magnitude of the pressure remains the same, the length of the pressure wave varies with each trial. Each pressure wave lasted 20 seconds, 15 seconds, 10 seconds, 5 seconds, and 2 seconds. These times were chosen because symptoms from strangulation arise within 5 to 10 seconds of force being applied. The duration was increased by increments of 5 up to 20 seconds. The exception was the 2-second wave, which was used to test the effects of a 1-second pressure wave while keeping one extra second to return to resting pressure. A plot of these five pressure waveforms can be found in **Figure 6**. Additionally, since the pressure wave requires an indefinite amount of time to return to resting pressure, each wave included one whole second to return to the resting pressure of 2.666E-3 MPa. There was also a control trial that did not experience any pressure waveform and had a consistent pressure of 2.666 E-3 MPa, which was used to compare the stress, deformation, and blood flow behavior.

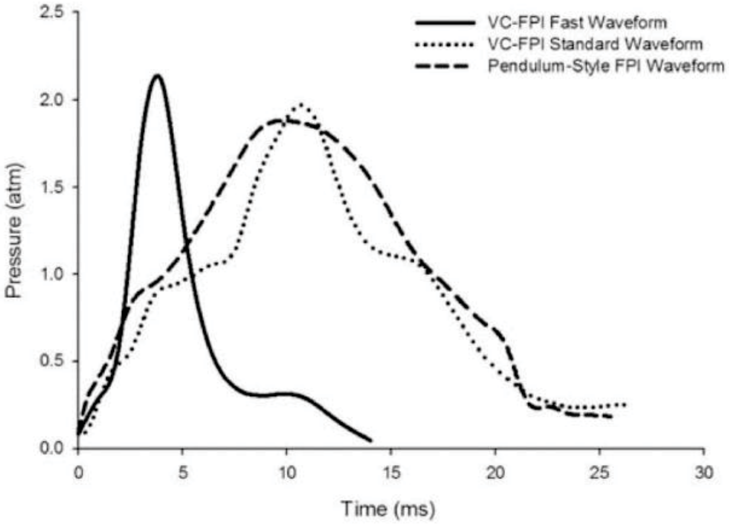

Figure 5: VC-FPI Pressure Waveforms, provided by Neuberger et al. Representative of fast- and standard-rise pressure waveforms administered during animal injuries using the VC-FPI device [28]

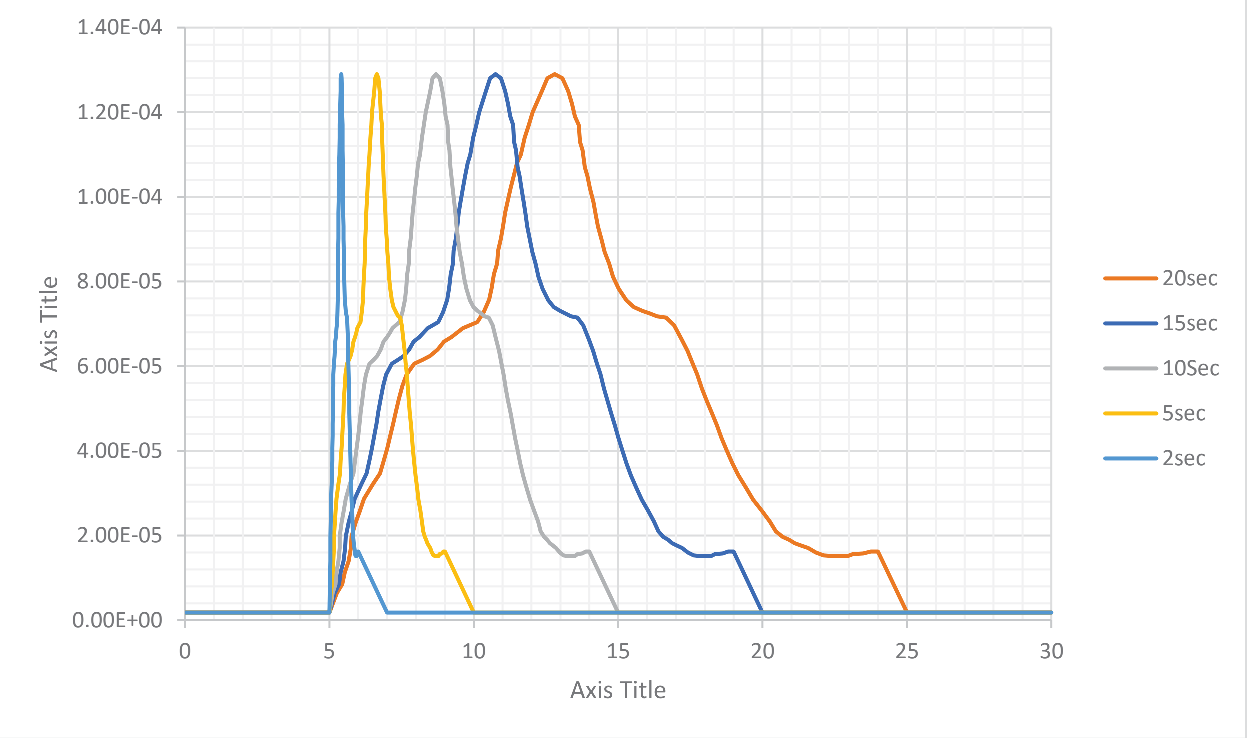

Figure 6: Pressure vs Time Plot for pressure waveforms of varying durations

In addition to Neuberger's pressure wave changing in duration, the magnitude of the pressure wave was also modified. The magnitude of the 10-second pressure wave was multiplied by a factor of 0.2, 0.4, 0.6, and 0.8 for these pressure waves. The magnitude was the difference between the resting pressure and the pressure wave value. The plots of all five pressure waves compared to the control can be found in **Figure 7.** The pressure waves of varying magnitude were compared to the control setting and full 10-second pressure wave. The 10-second pressure wave was used because the applications of strangulation force can cause loss of consciousness and other bodily functions in as little as 5 and 10 seconds [5]. As such, the 10-second wave was selected because it falls within the upper limit for those values. The pressure increases from a factor of 0 to a factor of 1 in increments of 0.2. The factor of 0 serves as the control, while the factor of 1 is the original magnitude of the pressure.

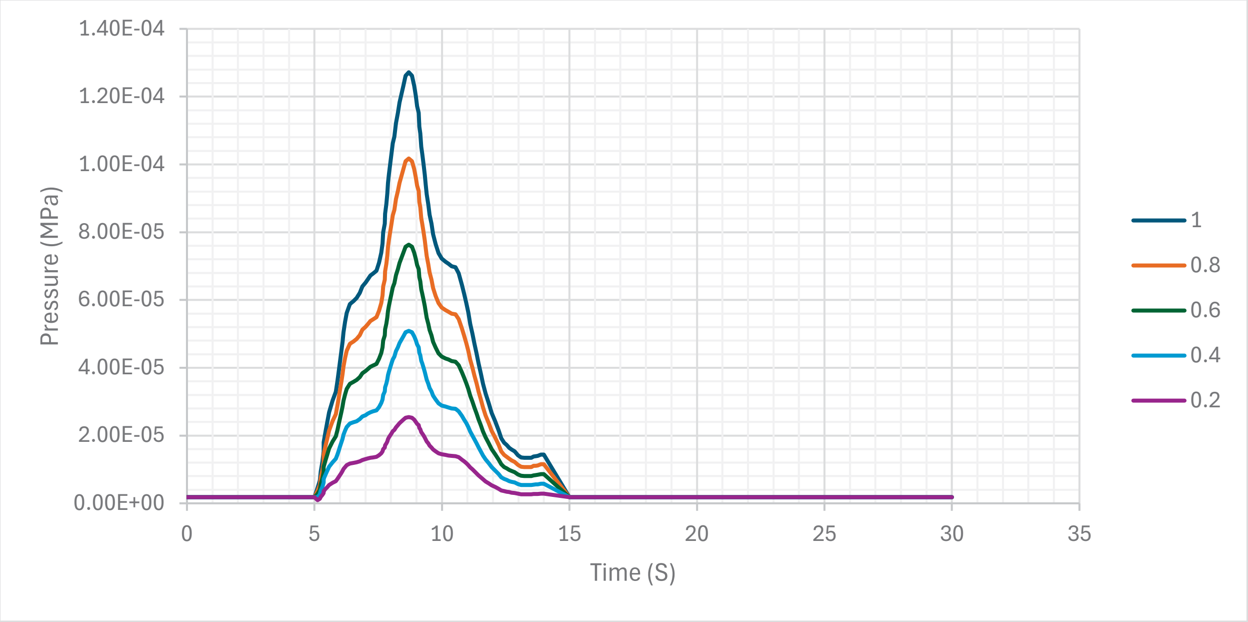

Figure 7: Plot of the 10-second pressure wave with varying magnitude of different factors

System Coupling

After the Transient Structure and Fluent components were defined, the setups of both components were processed through the ANSYS System Coupling feature. The System Coupling allows for a two-way fluid-solid interaction between the Transient Structure and Fluent components through data transfers such as force, displacement, heat, etc. [30]. The fluid inside the vessel generated pressure onto its inner wall as it flowed. Meanwhile, the pressure wave is exerted on the outer wall of the vessel, normal to each face of the vessel solid. This applies stress to the vessel and causes it to deform. But before the system coupling could run, the analysis settings for the Transient and Fluent components had to be defined. This experiment would end after 30 seconds and have a time step of 1 second with four iterations every second. This means that there are about four calculations per second for 30 seconds. While increasing the time step is possible for finer time measurements, computational limits must be considered for the time allotted for this study. Once both components are ready for coupling, their "setup" features are bound to that of the System Coupling component. A snapshot of the ANSYS workbench with all three Components can be seen in **Figure A2** in the **Appendix**. Inside the System Coupling component, 2 data transfers were added to couple the effect the vessel wall had on the fluid and vice versa. This allows the two components to interact with each other during the simulation.

Results

Following the ANSYS iterative simulation, the program could output different variables, most notably equivalent stress (ES), total deformation (TD), and fluid velocity. These were recorded using the measuring software built into the ANSYS program. Because the pressure waveform was compressed and altered for each trial, each one experienced its peak pressure and different points in time. Likewise, the measurements in the tables were taken at each of the trial's respective peaks in pressure. For the variation in magnitude, the measurements of TD, ES, velocity, and pressure were taken simultaneously as they share peak pressure timing.

Variation in Duration

Equivalent stress

ANSYS uses the Von Mises Stress equation to record the vessel's equivalent stress. This was accomplished by recording the three-dimensional stresses of an element. Ordinarily, each element of the solid structure would experience a complex stress state that can be transcribed as a 3x3 tensor, as seen in **Equation 4.** This provides nine different values of stress for each element. ES Once acquiring the nine components of stress, ANSYS uses the Von Mises Stress formula to provide a scalar value for the stress the vessel endures based on **Equation 5**, provided by the ANSYS online manual [31]. While the von Mises Stress is traditionally used for more ductile materials like steel, the result should still be relevant for the hyperelastic material of the vessel. **Figure 8** show how each element experiences ES in the ANSYS viewer.

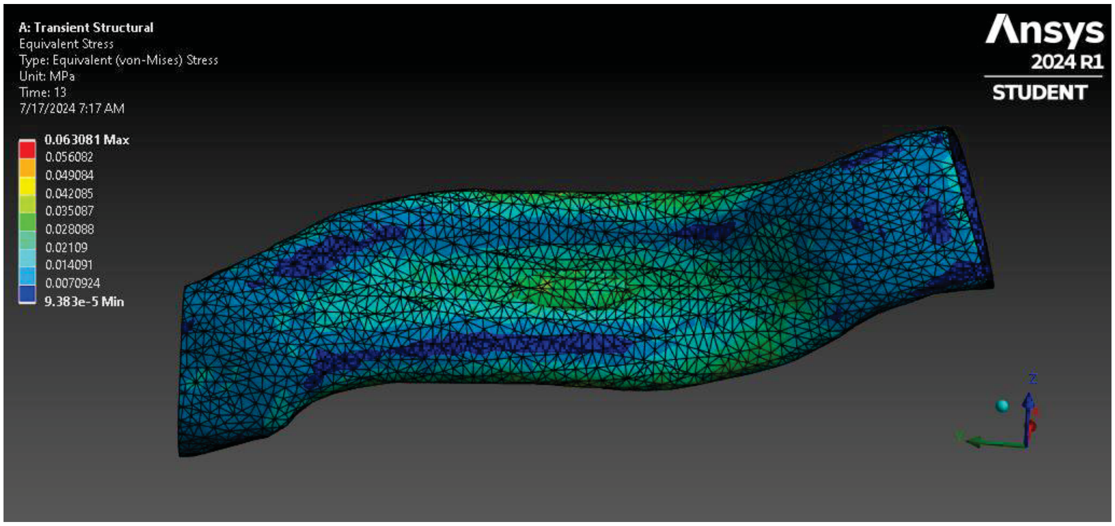
A: Transient Structural
Equivalent Stress
Type: Equivalent (von-Mises) Stress
Unit: MPa
Time: 13
7/17/2024 7:17 AM

Figure 8: ANSYS view of Equivalent stress and peak pressure wave of the 20-second pressure wave.

ANSYS records the minimum, maximum, and average ES at each specific step in time, meaning the maximum, minimum, and average are relative to the 3D space, not the overall time. For example, the maximum ES is the element that experiences the most stress through the model at a particular time step. The minimum is the same, except it is the element that experiences the least amount of ES. The average ES is the total ES divided by the number of elements present within the mesh.

$$\begin{bmatrix} \sigma_{xx} & \sigma_{xy} & \sigma_{xz} \\ \sigma_{yx} & \sigma_{yy} & \sigma_{yz} \\ \sigma_{zx} & \sigma_{zy} & \sigma_{zz} \end{bmatrix} \tag{4}$$

$$\sigma_v = \sqrt{\frac{\left(\sigma_{xx}-\sigma_{yy}\right)^2+\left(\sigma_{yy}-\sigma_{zz}\right)^2+(\sigma_{zz}-\sigma_{xx})^2+6\left(\sigma_{xy}^2+\sigma_{yz}^2+\sigma_{zx}^2\right)^2}{2}} \tag{5}$$

Total Deformation

Total deformation (TD) was calculated based on an element's X, Y, and Z displacement from its original position. TD is the square root of the total of the square of the X, Y, and Z directions as provided by **Equation 6** [32]. In the case of ANSYS, it provides minimum, maximum, and average deformation of the solid structure. Like ES, these values are minimum, maximum, and average deformations and a single point in time, not throughout the entire simulation. Unlike ES, the minimum deformation will always be 0 mm regardless of the simulated variable or point in time. Due to the minimum deformation being zero for each trial, minimum deformation was omitted from the records. The maximum and average deformation of the vessel at peak pressure can be found in **Table 6**.

$$TD = \sqrt{X^2 + Y^2 + Z^2} \tag{6}$$

Deformation is an essential factor to consider. Measuring deformation helps determine the stress and strain that the vessel may endure during the simulation. Additionally, this can be translated into clinical models. Vessels are usually anchored to some other structure within the body. As such, deformation can impact not only the vessel itself but also the adhering tissue. While this study assumed the vessel was freely suspended in CSF, future research involving intracranial tissue will find the deformation of a vessel crucial, especially considering how sensitive intracranial tissue is. An image of how each element experiences different TD can be found in **Figure 9**.

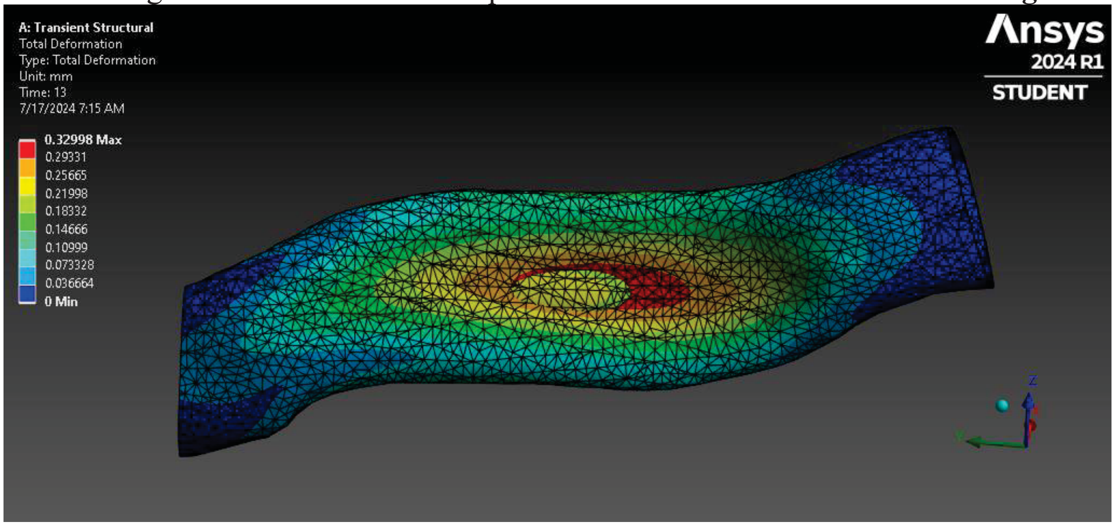

Figure 9: ANSYS viewer of vessel at peak Total Deformation during the 20-second pressure wave.

Blood Velocity

ANSYS recorded the vessel's Equivalent Stress and Total Deformation and the velocity and flow of the blood within it. Like ES and TD, each trial experienced maximum velocity at the second of peak pressure. The maximum blood flow velocity was also taken at the approximate middle along the vessel's length.

The velocity of the fluid flowing through the vessel was measured using two different methods. The first method used the contour feature in the Post-Processing component of ANSYS. This feature measures and displays the velocity profile along a plane after the simulation. Five contours were generated along the vessel for each trial. Each was offset by 3 mm from the other. The third contour was placed in the middle of the vein to record the maximum velocity of the fluid and provide the shape of the lumen during the simulation.

The first contour map is the control trial, as seen in **Figure 10**. It serves as the baseline for the remaining trials. The gradient range for the contours ranges from 0 to 28 cm/s. This range remains constant throughout the entire post-processing period between the contours and the streamlines. The center contour was the primary focus of the research as it experienced the most deformation. Therefore, it experienced the most change in velocity magnitude and profile.

It is also important to note that the contours were recorded in 3 instances. The first instance was 5 seconds after the simulation started. As stated earlier, there was a 5-second grace period before the pressure wave was initiated to allow the system to acclimate to itself. As such, the 5-second mark was used as the initial condition for the simulation. The next instance was the point of maximum TD and ES, which occur simultaneously as the maximum pressure. This is also the approximate point in time where the pressure waveform reaches its maximum magnitude, round to the nearest second to the ANSYS iteration setup. Nevertheless, this point of maximum TD and ES is also the point of maximum velocity, which varies based on trial and pressure wave deformation. The final instance was 30 seconds after the simulation started. This was the end of the simulation and was chosen to study how the vessel might respond to the different durations of pressure waves. Unfortunately, the maximum velocity and profile of the contours return to that of the initial state.

Five contours were added to each trial. The outlet of each trial is marked by the dark ellipsoid in **Figures 11, 12, 13, 14, 15**. Likewise, these figures show that each center contour experiences a different velocity and profile based on the duration of the pressure wave. The contours were measured at 3 different instances for each trial. The first instance was the 5-second mark. Last was the 30-second mark. The second instance was at the peak of each trial, which varied. **Figure 11** shows the velocity contours of the trial with the 2-second wave. Its peak was at 6 seconds. Next, **Figure 12** shows the velocity contours of the trial with the 5-second wave. Its peak was at 7 seconds. **Figure 13** shows the velocity contours of the trial with the 10-second wave. Its peak was at 9 seconds. **Figure 14** shows the velocity contours of the trial with the 15-second wave. Its peak was at 11 seconds. **Figure 15** shows the velocity contours of the trial with the 20-second wave. Its peak was at 13 seconds. Afterward, the vessel returns to its original, steady profile and magnitude. Unfortunately, all trials return to the same velocity profile and magnitude at the 30-second point. The tabulated value for the maximum velocity can be found in **Table 6.**

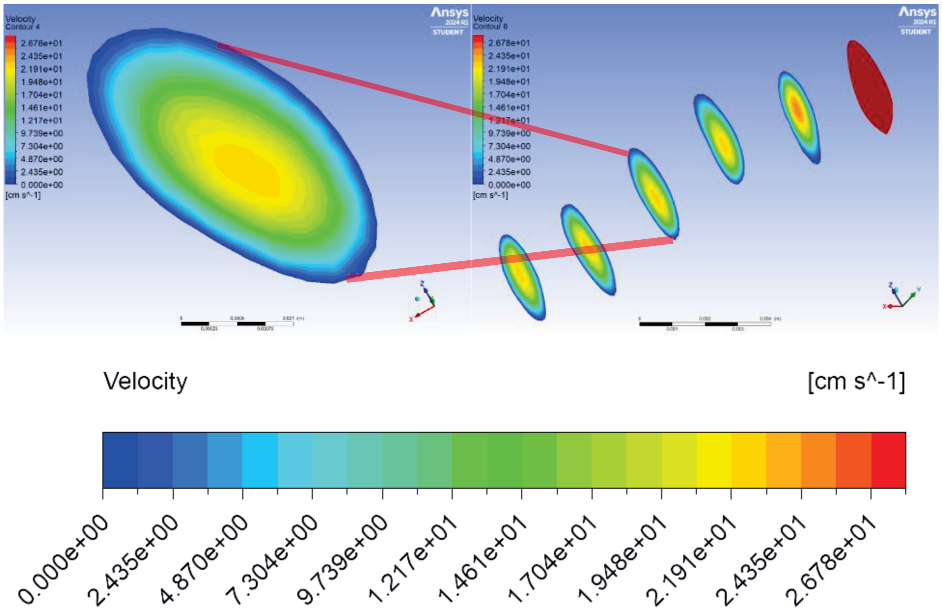

Figure 10: Velocity contours of the vessel under controlled conditions. The outlet profile is designated at the dark ellipsoid. No pressure wave was enacted upon the vessel. Left panel shows shape and gradient of middle contour.

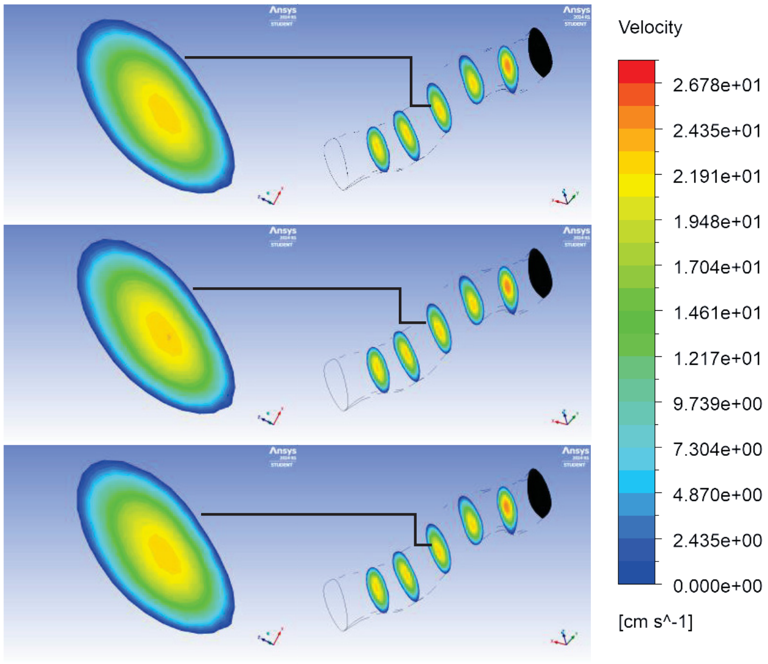

Figure 11: Contours of the 2-second waveform after 5 seconds (Top), 6 seconds (Middle), and 30 seconds (Bottom)

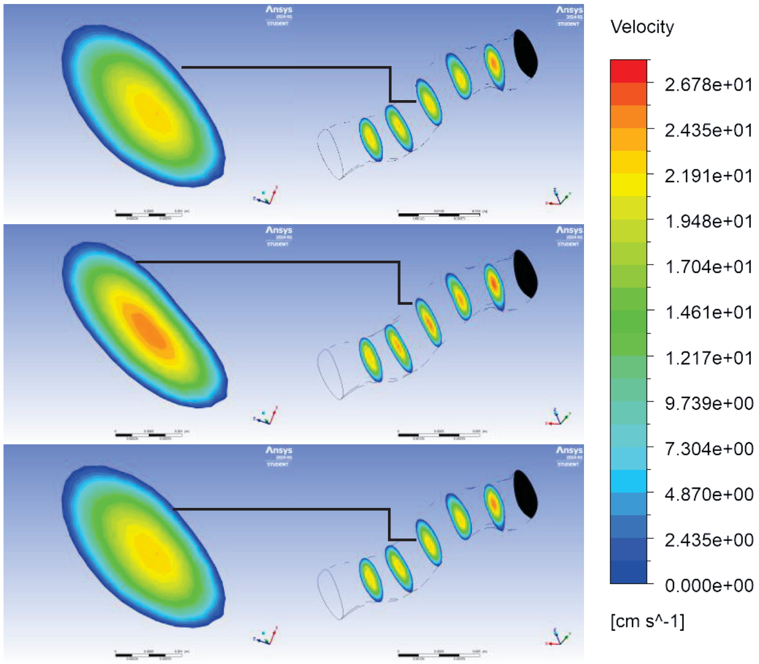

Figure 12: Contours of the 5-second waveform after 5 seconds (Top), 7 seconds (Middle), and 30 seconds (Bottom)

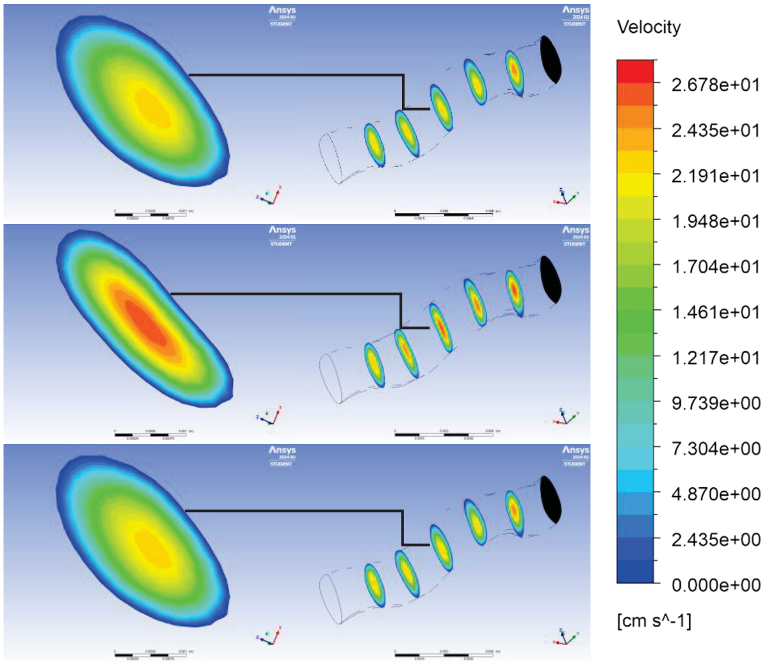

Figure 13: Contours of the 10-second waveform after 5 seconds (Top), 9 seconds (Middle), and 30 seconds (Bottom)

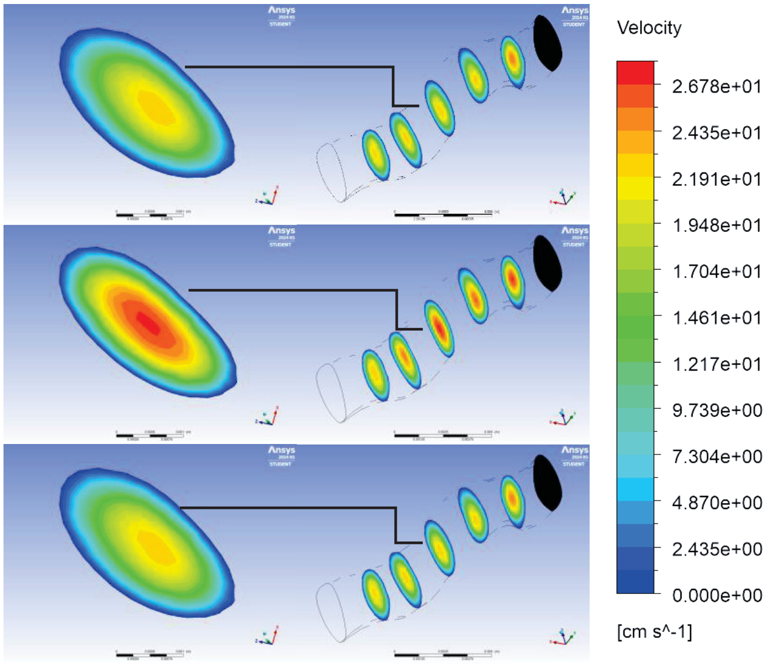

Figure 14: Contours of the 15-second waveform after 5 seconds (Top), 11 seconds (Middle), and 30 seconds (Bottom)

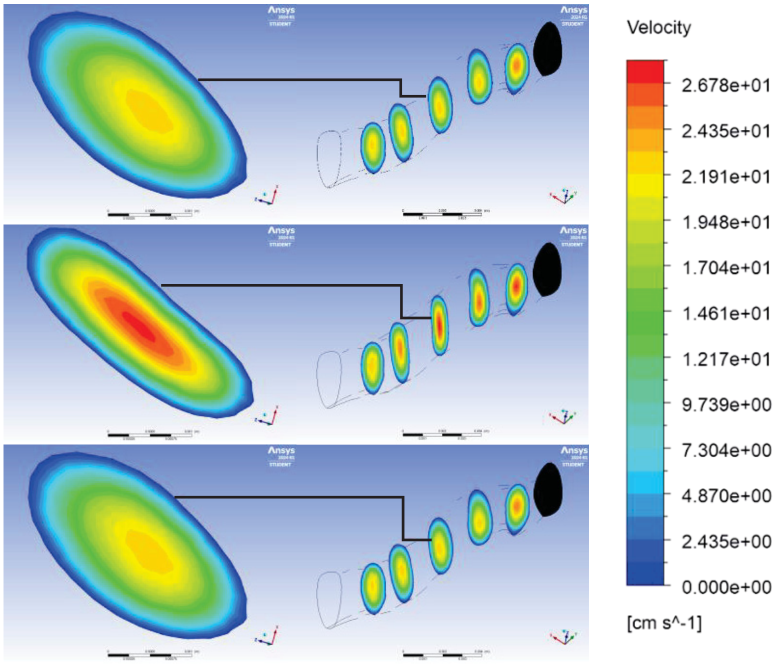

Figure 15: Contours of the 20-second waveform after 5 seconds (Top), 13 seconds (Middle), and 30 seconds (Bottom)

The next means of measuring velocity throughout the vessel was using the streamline feature in ANSYS. Streamlines allow us to see how the velocity changes longitudinally along the vessel. The program tracks a particle through the fluid volume and measures its velocity, drawing a path.

Figure 16 serves as the point of reference for the other trials. It provides the velocity streamlines for the blood within the vessel. There are 200 individual streamlines equally spaced in each trial. Like the contours, the streamlines across all images have a range of 0 to 28 cm/s. 2 angles were recorded to observe better the deformation enacted on the vessel. Unfortunately, due to the fidelity of the post-processing viewer, the change in the shape of the streamlines remains challenging to capture in images. This is because the deformation of the vessel remains difficult to see. However, the areas of the maximum velocity along the velocity remain quite visible, even in the following images. These images also helped determine the optimal locations for contours.

Figures 17 through **21** also show the change in velocity in each trail. Each image has 200 individual streamlines. **Figure 17** shows the velocity contours of the trial with the 2-second wave with its peak at 6 seconds. Next, **Figure 18** shows the velocity streamlines of the trial with the 5-second wave with its peak at 7 seconds. **Figure 19** shows the velocity streamlines of the trial with the 10-second wave with its peak at 9 seconds. **Figure 20** shows the velocity streamlines of the trial with the 15-second wave with its peak at 11 seconds. **Figure 21** shows the velocity streamlines of the trial with the 20-second wave. Its peak was at 13 seconds.

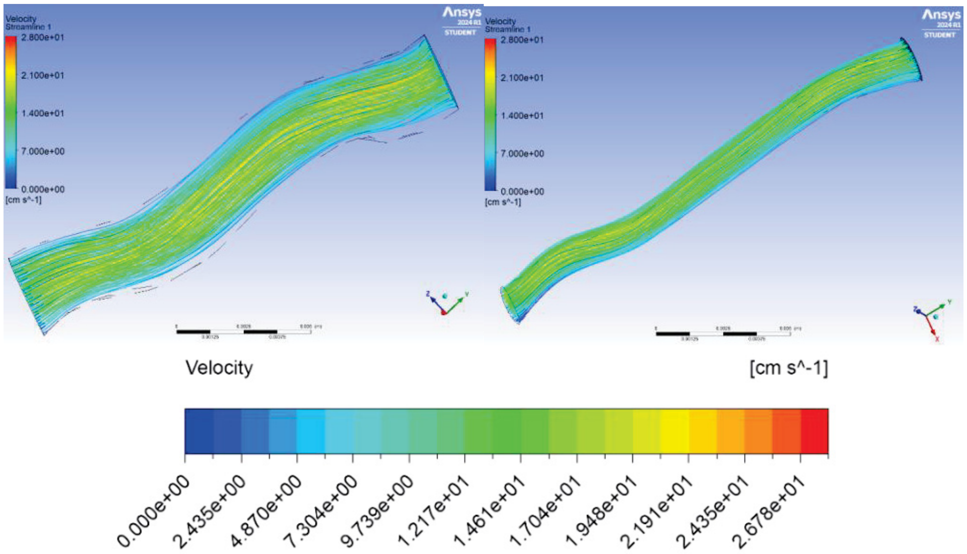

Figure 16: Streamline of Control Trial (Inlet in right corner of each image)

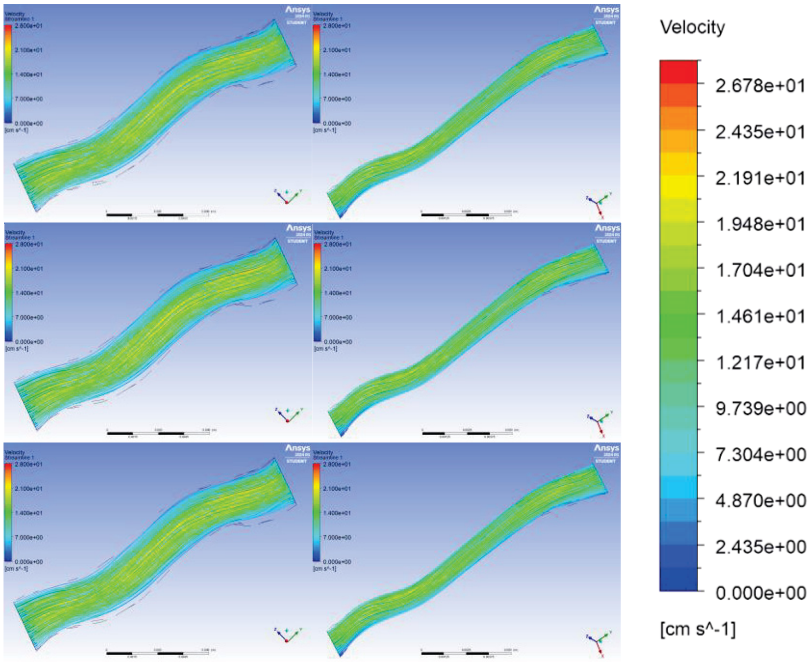

Figure 17: Streamline of the 2-second waveform from 2 angles after 5 seconds (Top), 6 seconds (Middle), and 30 seconds (Bottom) (Inlet in right corner of each image)

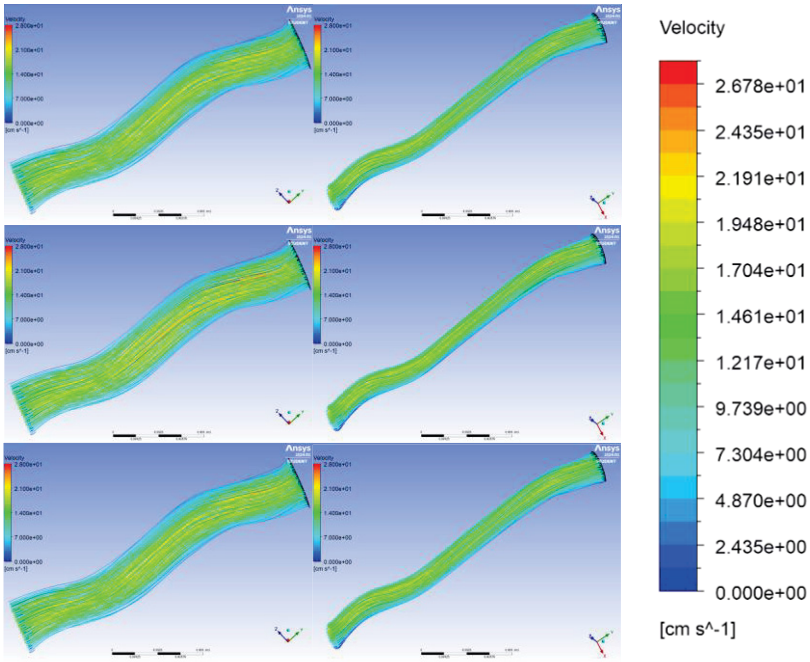

Figure 18: Streamline of 5-second waveform angles after 5 seconds (Top), 7 seconds (Middle), and 30 seconds (Bottom) (Inlet in right corner of each image)

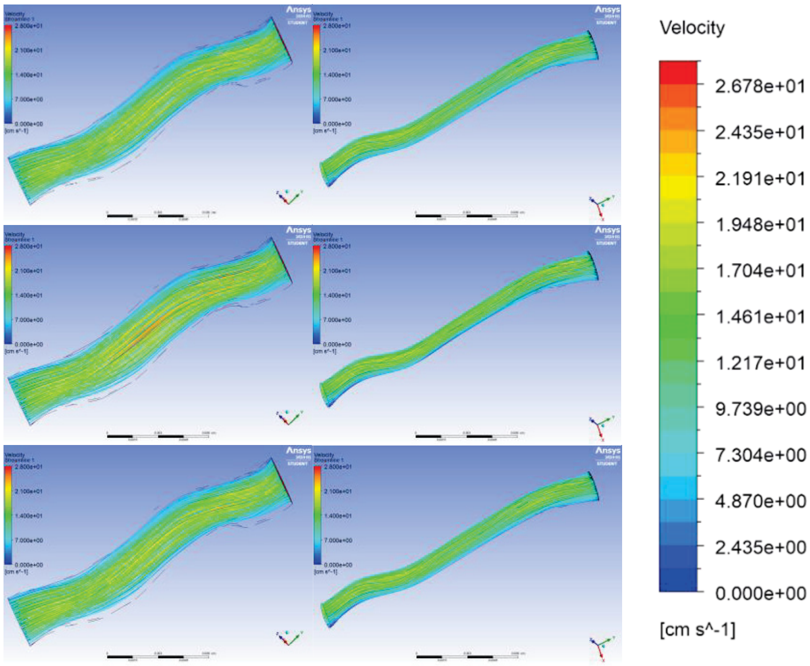

Figure 19: Streamline of 10-second waveform angles after 5 seconds (Top), 9 seconds (Middle), and 30 seconds (Bottom) (Inlet in right corner of each image)

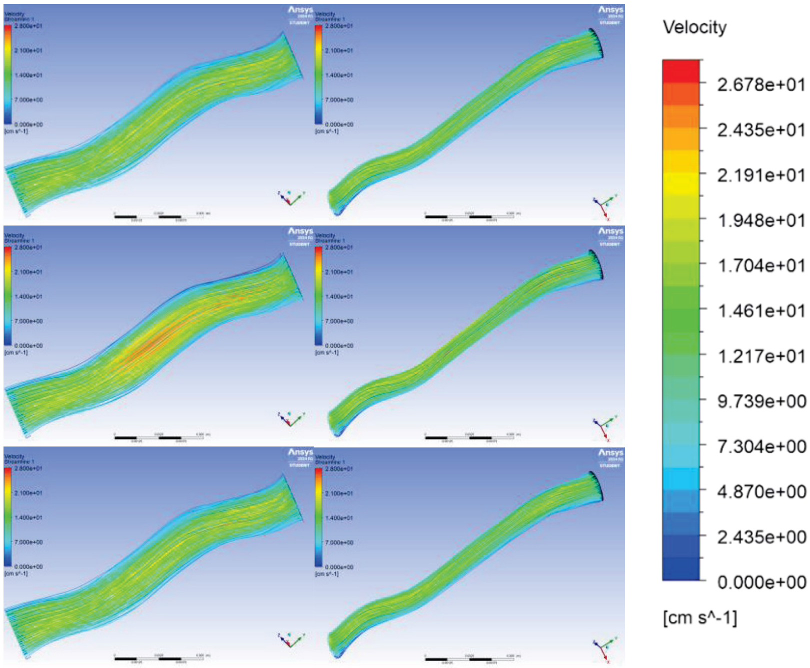

Figure 20: Streamline of 15-second waveform angles after 5 seconds (Top), 11 seconds (Middle), and 30 seconds (Bottom) (Inlet in right corner of each image)

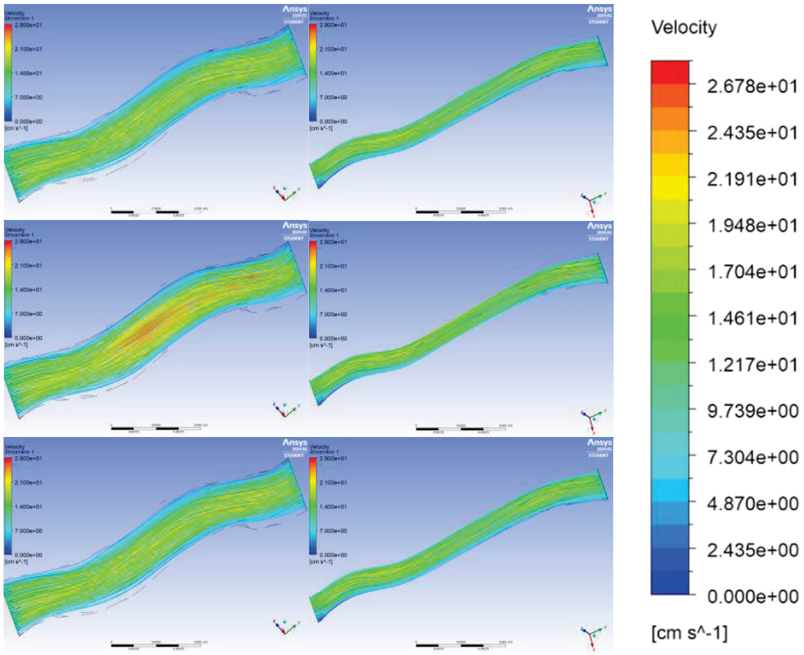

Figure 21: Streamline of 20-second waveform angles after 5 seconds (Top), 13 seconds (Middle), and 30 seconds (Bottom)(Inlet in right corner of each image)

Fluid Pressure

The next part of the study, which examines the variation in duration, is the fluid pressure. The pressure was plotted to facilitate blood flow analysis, as determining blood velocity is much more complicated than measuring blood pressure. The change in fluid pressure over time is plotted in **Figures 22** and **23**. **Figure 22** shows the average static pressure of the fluid volume over time. **Figure 23** shows the average dynamic pressure of the fluid volume over time. Static pressure is the pressure of the fluid volume regardless of velocity, while dynamic pressure is the pressure based on the velocity and flow rate of the fluid [33]. The peak static and dynamic pressures were recorded in **Table 6**. An essential item to note is the fact that static pressure is negative. This is because total pressure decreases as the velocity increases. Likewise, as dynamic pressure increases with velocity, static pressure must decrease to compensate for this to maintain the algebraic sum of potential energy, kinetic energy, and pressure constant [34] [35]**.** This operates on Bernoulli's principle, which can be seen in **Equation 7** [26]**.** **'**P' represents the static pressure, 'ρ' is density, 'V' is velocity, 'g' is gravity, and 'C' is a constant. Due to static pressure being negative, its peak was assumed to be its minimum, while the dynamic pressure peak was its maximum.

$$p + \rho\frac{V^2}{2} + \rho g z = C \tag{7}$$

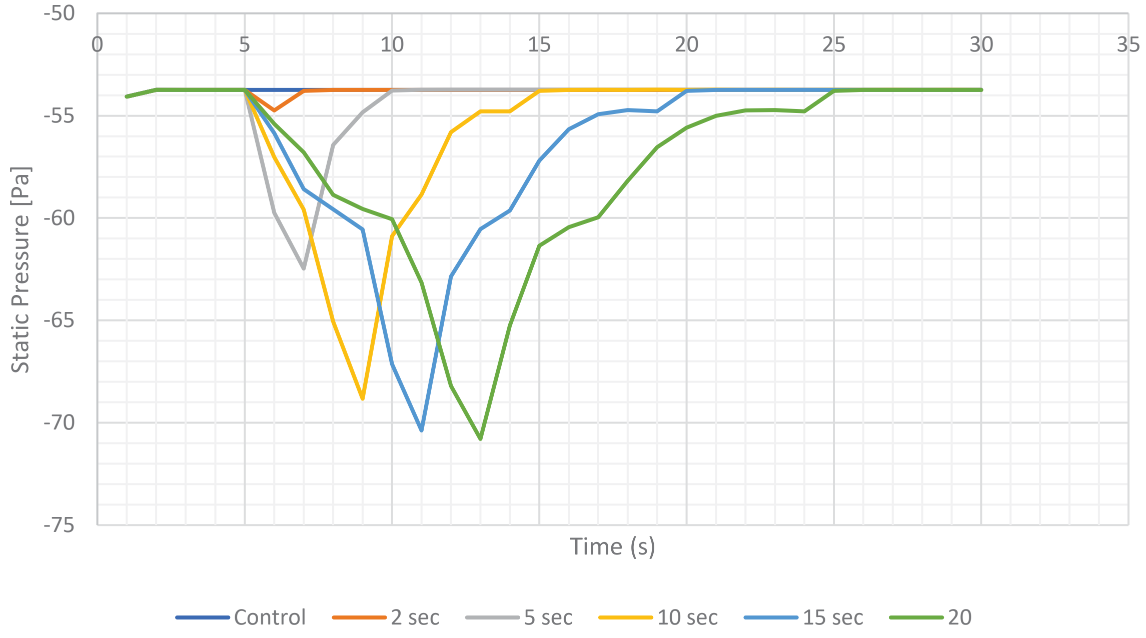

Figure 22: Average Static Pressure of fluid volume over time

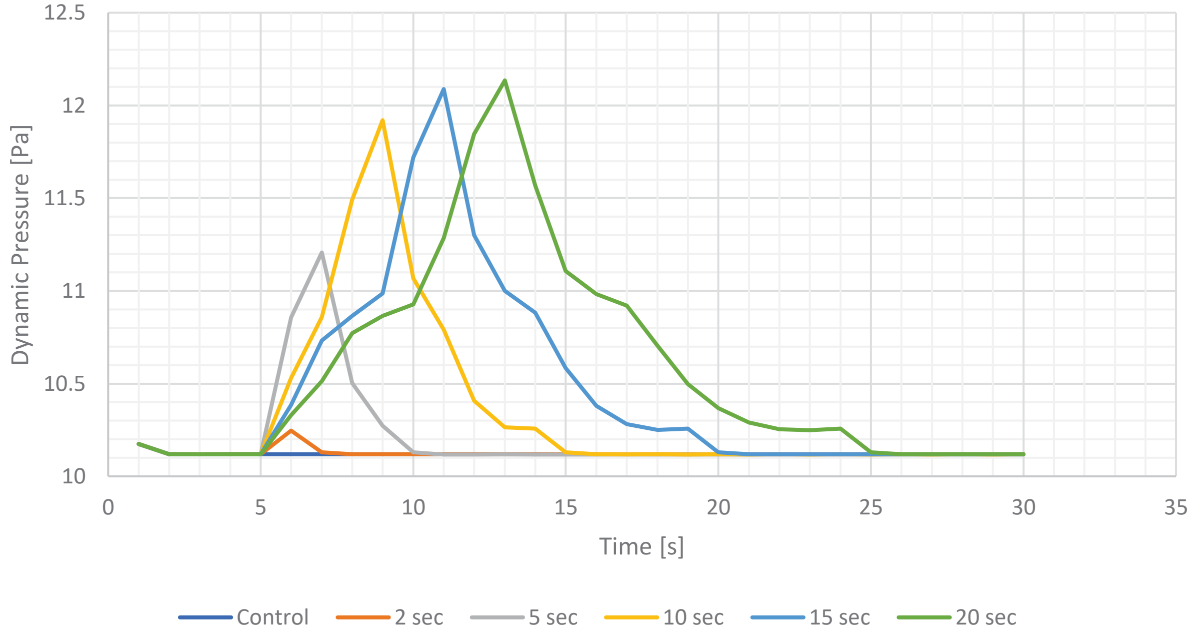

Figure 23: Average Dynamic Pressure of fluid volume over time.

Table 6: Deformation, Stress, and Pressure values of simulation by pressure waveform duration

Length of Pressure Wave (seconds)	0 (control)	2	5	10	15	20
Max Deformation (mm)	0.065366	0.088448	0.22605	0.30873	0.32572	0.32998
Average Deformation (mm)	0.019888	0.026202	0.063591	0.085316	0.089669	0.090759
Min Stress (MPa)	9.384E-05	1.270E-04	3.710E-04	5.060E-04	5.170E-04	5.220E-04
Max Stress (MPa)	1.221E-02	1.655E-02	4.307E-02	5.908E-02	6.228E-02	6.308E-02
Average Stress (Mpa)	3.164E-03	4.104E-03	9.636E-03	1.284E-02	1.348E-02	1.364E-02
Max Velocity (cm/s)	22.8892	23.2284	25.1289	26.7272	27.1189	27.2154
Peak Static Pressure [Pa]	-54.0642	-54.7445	-62.4692	-68.8271	-70.3768	-70.7906
Maximum Dynamic Pressure [Pa]	10.173955	10.24666	11.20725	11.92065	12.0884	12.13511
Time of Peak Pressure (sec)	NA	6	7	9	11	13

Variation in Magnitude

Equivalent Stress

Using the Von Mise Stress equation, the ES was calculated based on variation in pressure magnitude. The minimum, maximum, and average ES were recorded like the simulations with varying durations. However, they were all recorded at the same point in time due to the time of peak pressure being constant throughout the trials. **Table 7** shows the tabulated values of the ES**.**

Total Deformation

Using the TD formula, the TD of each vessel was calculated and recorded based on the variation in pressure magnitude. Like ES, the peak TD occurs at the same instance in time for each trial. **Table 7** shows the maximum and average TD values**.**

Blood Velocity

The simulations for the varying pressure wave also yield interesting results. **Figure 24** shows the change in velocity contours for the varying pressure magnitudes. The velocity contours were taken 9 seconds after the start of the simulation, as they all share the timing of maximum pressure from the external pressure wave. Likewise, the middle contour was used for the maximum velocity value. The tabulated values of the velocity can be seen in **Table 7.**

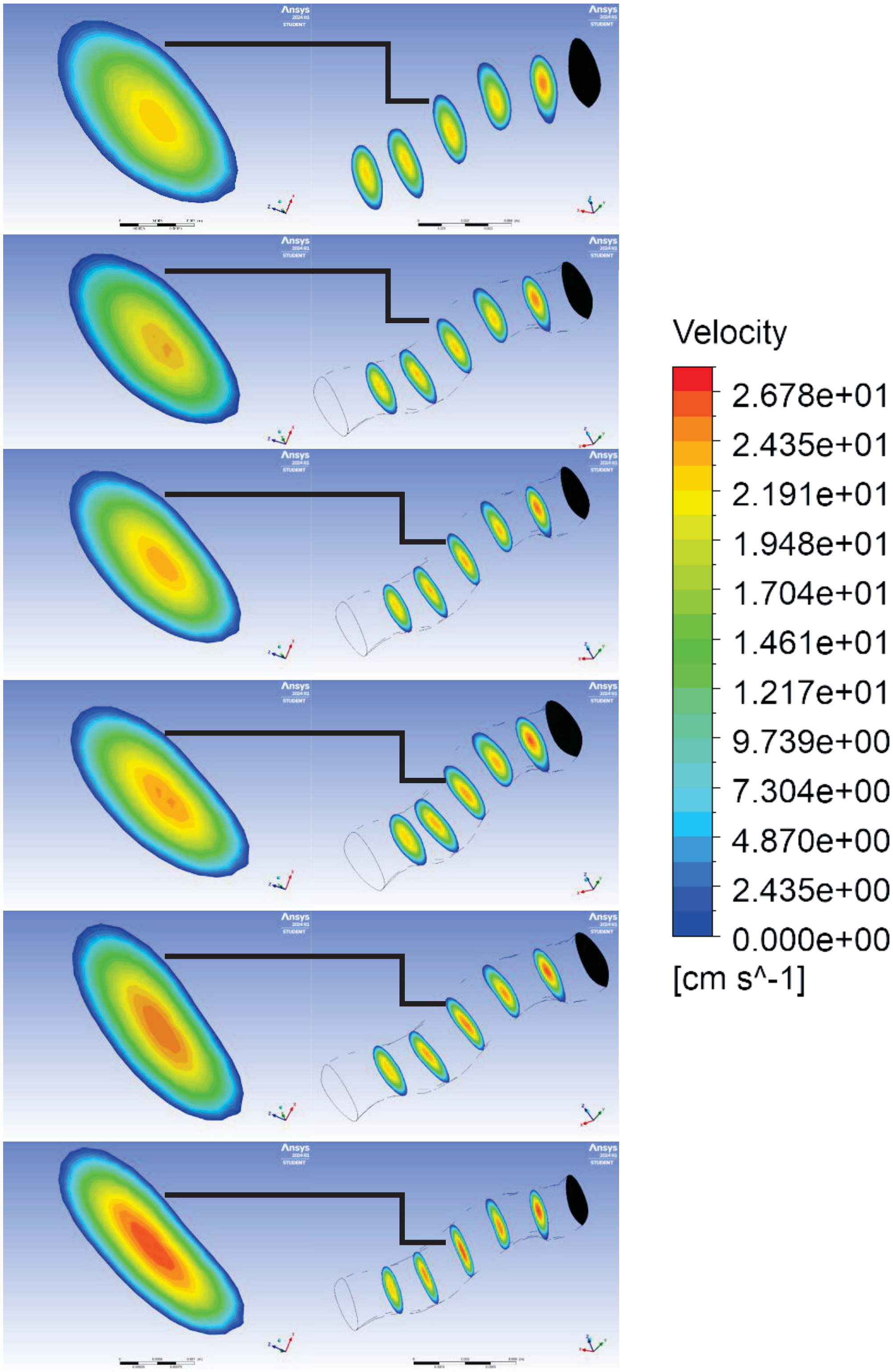

Figure 24: Contours of Varying Pressure magnitudes (Form Top to Bottom: 0 (control), 0.2, 0.4, 0.6, 0.8,) 1)

Fluid Pressure

Like the varying duration, altering the pressure magnitude affected the fluid pressure of the vessel. **Figure 25** shows the volumetric Average static pressure of the fluid from between 1 and 30 seconds of the simulation. **Figure 26** shows the volumetric average of the dynamic pressure over time. Both plots start at 1 second because the first second is spent initializing the simulation. In this case, the first 5 seconds of the simulation are negligible due to the time being used to have the simulation reach a steady state before the external pressure is enacted. The measurements were also taken as gauge pressure. The peaks of each pressure plot were recorded and tabulated in **Table 7.** Due to negative static pressure, its peak was assumed to be its minimum, while the peak of the dynamic pressure was its maximum.

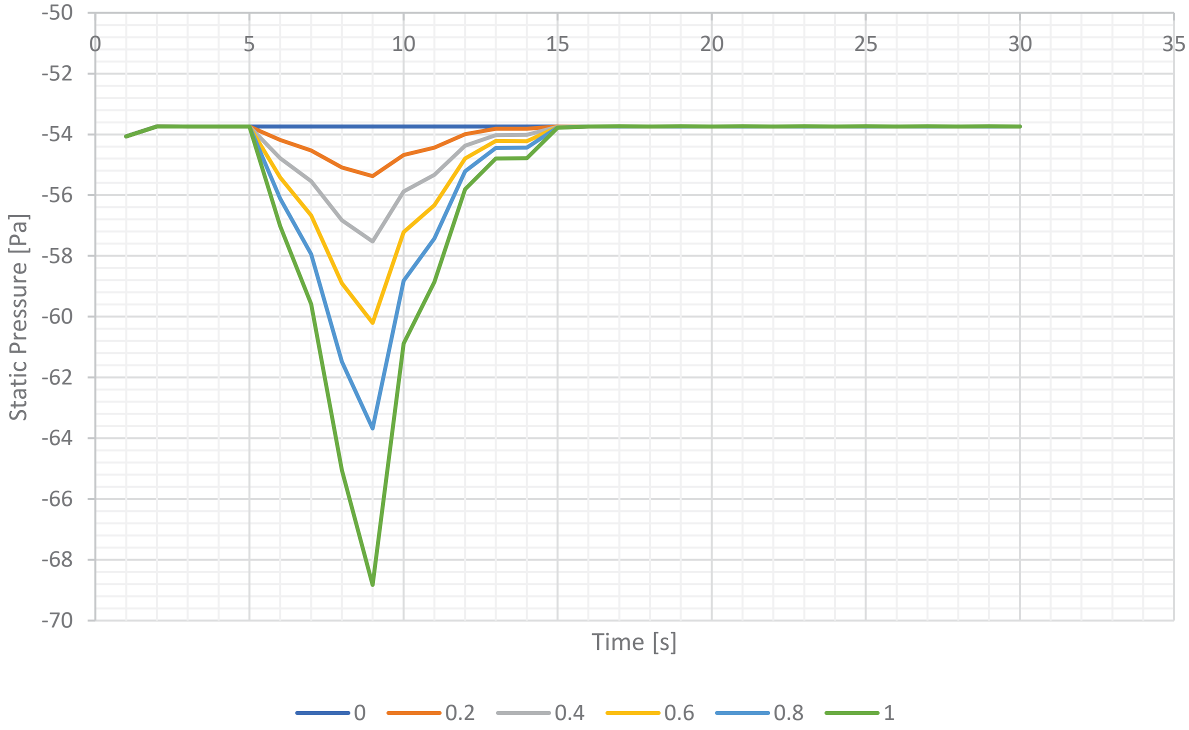

Figure 25: Volumetric Average of Static Pressure over time of varying Pressure Magnitudes

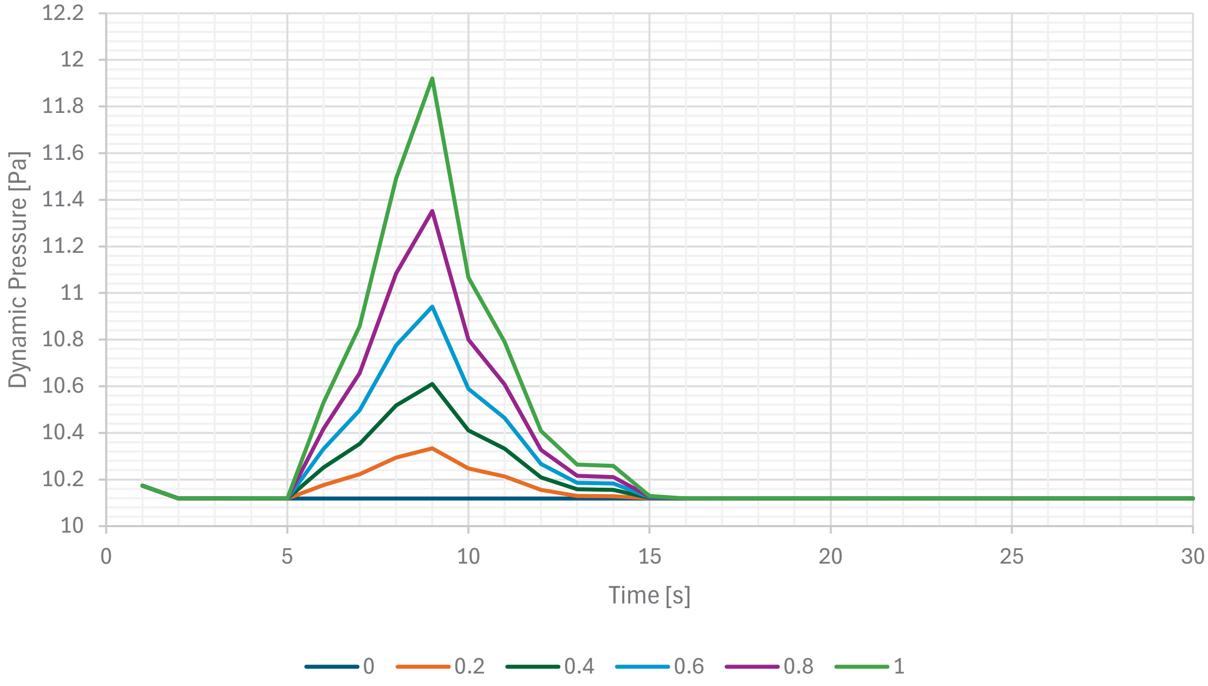

Figure 26: Average Dynamic Pressure over time of varying Magnitudes

Table 7: Velocity and Pressure of varying Pressure Magnitudes

Magnitude Factor of Pressure Wave	**0 (control)**	**0.2**	**0.4**	**0.6**	**0.8**	**1**
Max Deformation (mm)	0.065366	0.1012	0.14367	0.19043	2.43E-01	0.30873
Average Deformation (mm)	0.019888	2.97E-02	4.13E-02	5.40E-02	6.81E-02	0.085316
Min Stress (MPa)	9.38E-05	1.76E-04	2.53E-04	2.47E-04	4.75E-04	0.000506
Max Stress (MPa)	0.012213	1.90E-02	2.71E-02	3.61E-02	4.64E-02	0.059081
Average Stress (MPa)	22.8892	23.3458	23.8559	24.5303	25.4476	26.7272
Peak Static Pressure (Pa)	-54.06417	-55.3751	-57.5256	-60.2043	-63.6785	-68.8271
Maximum Dynamic Pressure (Pa)	10.1739	10.3338	10.6097	10.9417	11.35205	11.9206

Discussion

The simulation's vasculature and fluid models have provided a distinctive precedent for future intracranial pressure studies. This experiment can be divided into two distinct components. The first component was the Transient Structural component of the vessel itself. The second model is the Fluent component with the actual blood. Each component yielded unique and valuable data that may benefit future research in studying NFS.

Following the ANSYS simulation, the transient structural variables, ES and TD, of the simulations with varying durations were compared to the control trial. Despite the few data points, increasing the pressure duration or magnitude positively correlates to increasing all ES and TD values. As the duration of pressure increases, the maximum TD, average TD, minimum ES, maximum ES, and average ES all increase with the pressure duration. The increase in values is highly significant. The longest pressure wave duration can increase the value of a transient structural variable by up to 456.28%. **Figure 27** shows that the structural variables all have logarithmic behavior as the duration of the pressure wave increases [36]. An example of this can be seen in the curve fit for the maximum TD with an R^2 value of 0.9481. In a similar case, the ES and TD increased as the magnitude of the pressure wave increased. However, they increased at a second-degree power rate. An example of this can be seen in the curve fit for the maximum TD with an R^2 value of 0.9997. The plot for these values can be seen in **Figure 28**. There was an anomaly with the behavior of the minimum ES. This was most likely the result of an error from ANSYS when sampling the element with the lowest ES during the peak. The vessel may have deformed uniquely and caused a specific element to be under less stress than intended. Nevertheless, the average and maximum ES increased at a second-degree power rate.

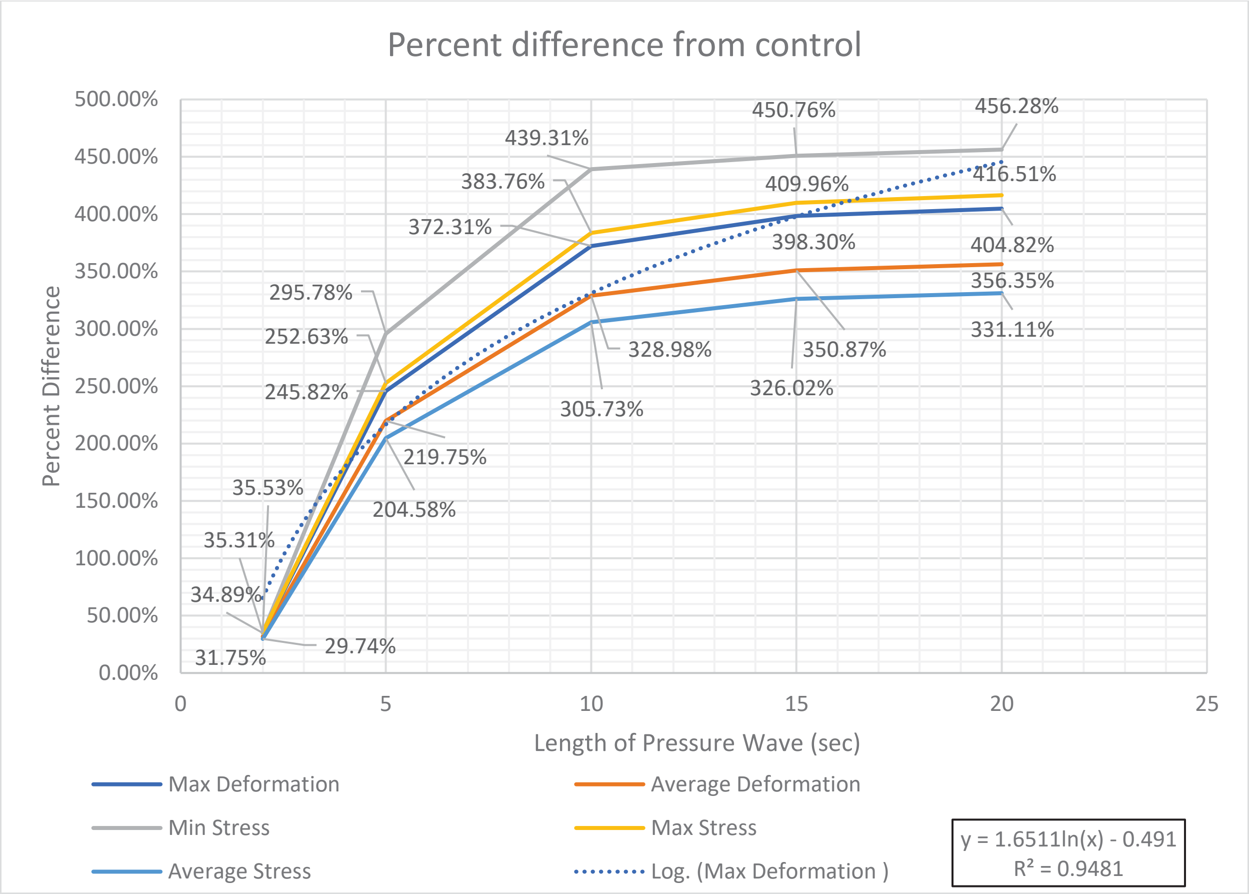

Figure 27: Percent Difference of Deformation and Stress of varying duration from Control Trial

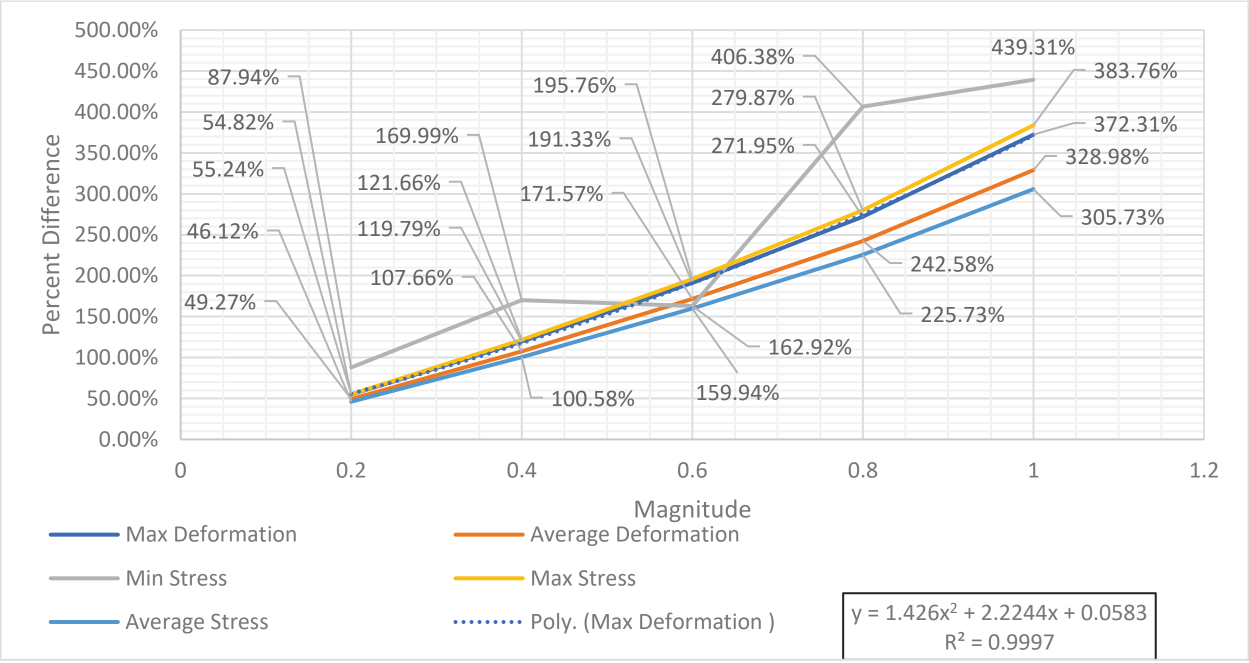

Figure 28: Percent Difference of Deformation and Stress of varying magnitude from Control Trial

The maximum velocity also incurred significant changes during the simulations of varying duration, but the change is nowhere near that of the transient structural variables. The maximum velocity only increases by 18.9% at most from changing the duration of the pressure. This increase was from the longest pressure duration of the entire experiment. Meanwhile, the maximum pressure increased by %16.77 at most during the trials of altering the magnitude of the pressure wave. There was also unique behavior when comparing the change in maximum velocity, as seen in **Figure 29**. The maximum velocity exhibited logarithmic change as the duration of the pressure wave increased. Meanwhile, the maximum velocity exhibited change resembling a second-degree curve as the magnitude of the pressure force was increased. Unfortunately, due to the lack of points, it is uncertain if they genuinely exhibit this kind of behavior. The percent change in the maximum TD, average TD, minimum ES, maximum ES, and average ES can be found in **Table 8.**

The maximum static and dynamic pressure also experienced significant changes during the study. While altering the duration of the pressure wave, the percent increase for a maximum dynamic pressure was 19.28 %, while the absolute value of the static pressure increased by 30.94%. For the simulation involving different pressure magnitudes, the maximum dynamic pressure increased by 17.17%, and the maximum static pressure increased by 27.31%. Like velocity, the two variables experience unique behaviors based on the pressure duration and magnitude change. As the pressure duration increases, dynamic and static pressure increases at a logarithmic rate. Meanwhile, increasing the magnitude of the external pressure wave causes the dynamic and static pressure to increase a second-degree power curve. While there were not enough trials to confidently determine the line of best fit for these relationships, the curve fitting for the data provided had R^2 values ranging from 0.9659 to 0.9993. The change in pressure and velocity based on duration and magnitude can be seen in **Figure 29** and **Figure 30**. The maximum dynamic and static pressure for the change in duration can be found in **Table 8.** The maximum dynamic and static pressure for the change in magnitude can be found in **Table 9.**

There was also the unique behavior based on the change in velocity along the vessel from the inlet to the outlet. Most notably, in **Figure 15,** the contours had an increase in overall velocity between the center and the inlet. This is most likely due to the compression of the vessel. Due to the irregular shape of the vessel, it does not deform uniformly. As such, the area between the inlet and center deforms more, thus experiencing more compression and less cross-sectional area. The decreased area causes the velocity to increase based on NSE [26]. The irregular compression would also explain the lower overall velocity in the contours between the center and the outlet. The vessel's cross-sectional area between the middle and outlet is greater than the space between the inlet and middle. This expansion of cross-sectional area immediately after a compression zone causes a drop in velocity; however, there is still compression compared to the resting state. As such, the overall velocity within the vessel increases, as seen by the colors of the contour map and data. The streamlines show a similar case, showing a greater velocity value between the middle and inlet during maximum compression.

Another interesting feature is the recovery of the vessel and fluid after the pressure wave. At the 30-second mark, all contours return to the resting state. The same applies to the volumetric fluid pressure, as the plots return to their original value, as seen in **Figures 22, 23, 25,** and **26**. While it is strange for the vessel to return to its resting state without repercussions after trauma, this study measures pressure, velocity, deformation, and stress. This study recorded the Von Mises Stress, which is usually compared to the material's yield stress to detect failure [31]. For intracranial veins, the axial yield stress is about 0.94 MPa. [37]. Assuming the vessel wall is isotropic, this value is far higher than the maximum equivalent stress from the study. However, this only indicates that the vessel will not burst or break from the pressure. Due to the vessel's biological nature, cellular damage is still possible. There is also the consideration of wearing out the vessel wall due to repeated instances of strangulation, which remains quite common.

Despite the intricacies of the simulation, there are still many shortcomings that will be acknowledged in future exploration of the field. First, there is the problem with aliasing and resolution. Due to processing power, the simulation only rounded to the nearest second with each recording, so there is a chance the maximum may be off due to missing them in the recorded data. There is also the need to validate this model, as physical models have yet to be tested with this.

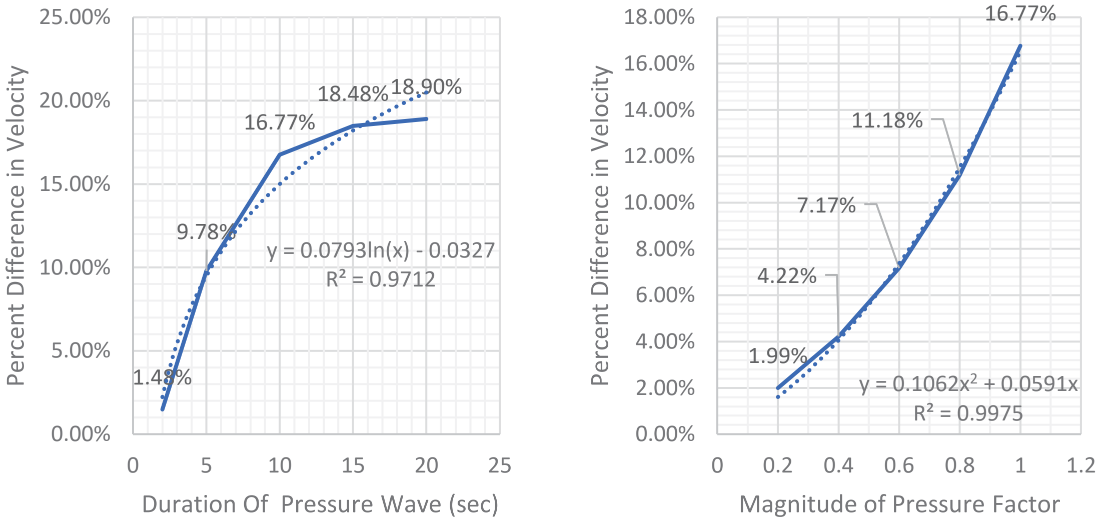

Figure 29: Percent Difference in maximum velocity based on the duration of pressure wave (left) and magnitude of pressure (right)

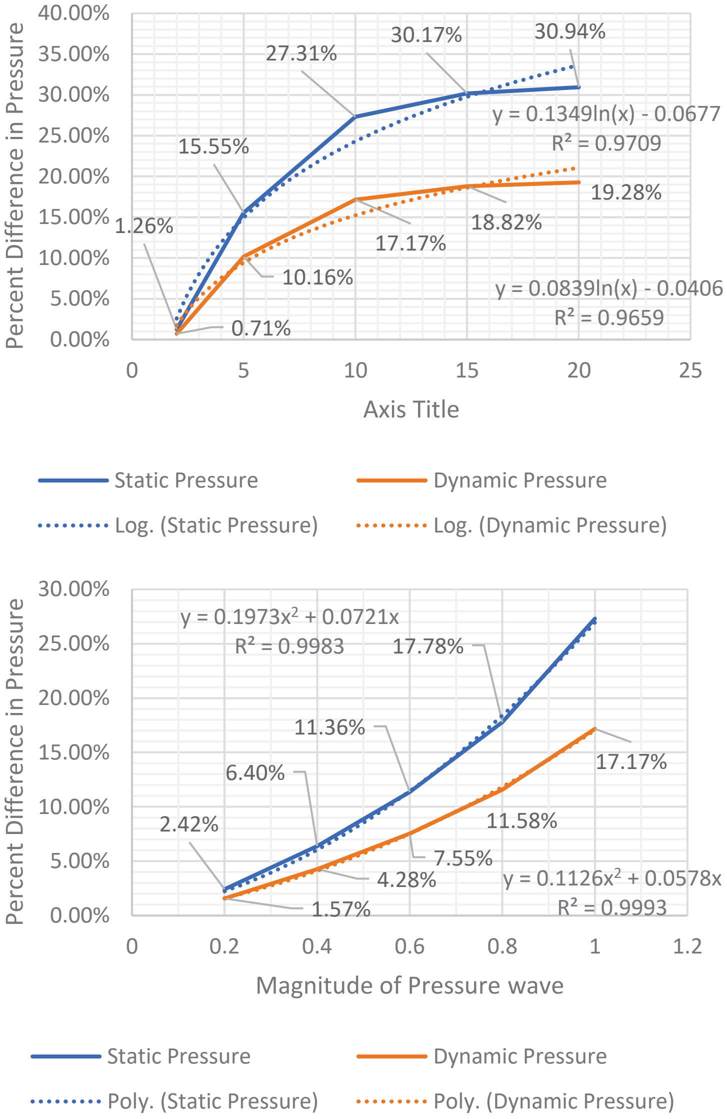

Figure 30: Static and Dynamic Pressure of varying durations (top) and varying magnitudes (bottom)

Table 8: Percent Difference from Control for Varying Durations

Duration of Pressure Wave	2	5	10	15	20
Max Deformation	35.31%	245.82%	372.31%	398.30%	404.82%
Average Deformation	31.75%	219.75%	328.98%	350.87%	356.35%
Min. Stress	34.89%	295.78%	439.31%	450.76%	456.28%
Max. Stress	35.53%	252.63%	383.76%	409.96%	416.51%
Average Stress	29.74%	204.58%	305.73%	326.02%	331.11%
Max Velocity	1.04%	9.97%	16.85%	18.42%	18.84%
Max Static Pressure	1.26%	15.55%	27.31%	30.17%	30.94%
Max Dynamic Pressure	0.71%	10.16%	17.17%	18.82%	19.28%

Table 9: Percent Difference from Control for Varying Magnitudes

Magnitude Factor	0.2	0.4	0.6	0.8	1
Max Deformation	54.82%	119.79%	191.33%	271.95%	372.31%
Average Deformation	49.27%	107.66%	171.57%	242.58%	328.98%
Min Stress	87.94%	169.99%	162.92%	406.38%	439.31%
Max Stress	55.24%	121.66%	195.76%	279.87%	383.76%
Average Stress	46.12%	100.58%	159.94%	225.73%	305.73%
Maximum Velocity	1.99%	4.22%	7.17%	11.18%	16.77%
Peak Static Pressure	2.42%	6.40%	11.36%	17.78%	27.31%
Maximum Dynamic Pressure	1.57%	4.28%	7.55%	11.58%	17.17%

Conclusion

This study focused on examining the effects of intracranial pressure on cerebral vasculature. The generated model and simulation provided excellent insight into the behavior of a cerebral blood vessel in the event of intracranial pressure. The study examined the effects of a surge in intracranial pressure on the stress and deformation of a diploic vein. Likewise, the study also provided data on the behaviors of the blood within the vessel, such as its pressure and velocity. While this only simulated a vein model, future models will study the impact of elevated ICP on an arterial model.

Summary

This study establishes a baseline model for future research on the effects of intracranial pressure on cerebral vasculature. NFS remains an understudied means of IPV. Likewise, it was one of the most insidious due to its difficulty in detection. By researching and studying its effect, I hope future researchers, forensics specialists, and medical professionals can better detect instances of NFS.

Appendix

Appendix A: DICOM scans

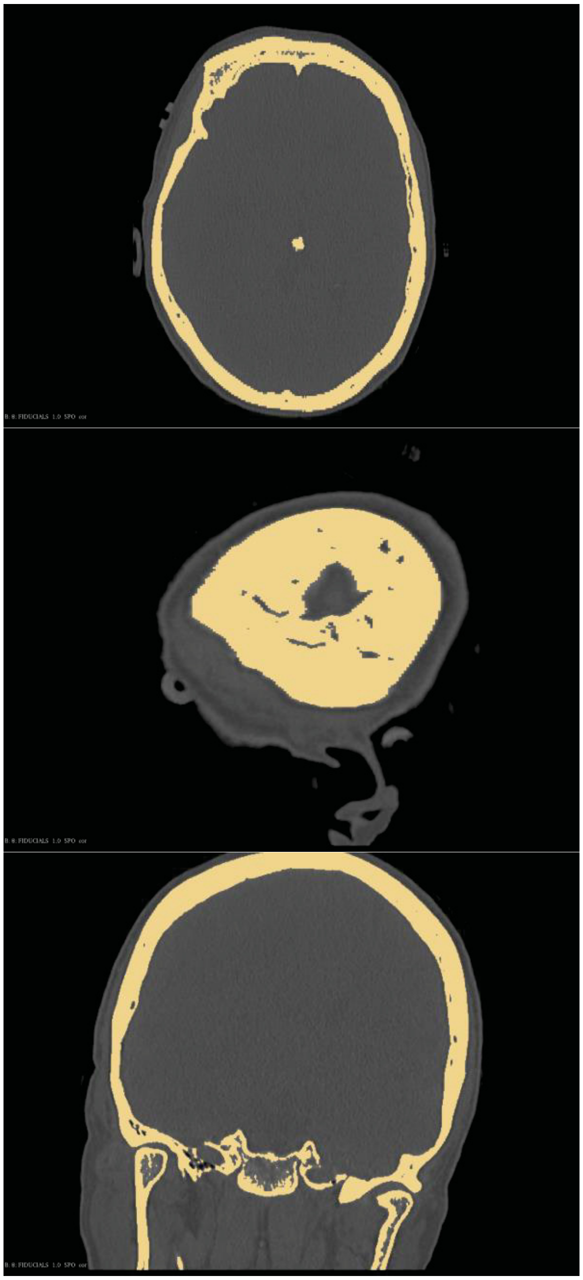

Figure A1

Appendix B: CT Metadata

```
[0008,0005]    SpecificCharacterSet     ISO_IR 100     CS   10
[0008,0008]    ImageType [4] DERIVED, PRIMARY, AXIAL, CT_SOM5
SPO  CS   34
[0008,0016]    SOPClassUID    1.2.840.10008.5.1.4.1.1.2     UI
     26
[0008,0018]    SOPInstanceUID
     1.3.6.1.4.1.14519.5.2.1.4591.4001.348019226599617584906520522050     UI   64
[0008,0020]    StudyDate 20080311  DA   8
[0008,0021]    SeriesDate     20080311  DA   8
[0008,0022]    AcquisitionDate     20080311  DA   8
[0008,0023]    ContentDate    20081114  DA   8
[0008,0030]    StudyTime      TM   0
[0008,0031]    SeriesTime     161133.609000  TM   14
[0008,0032]    AcquisitionTime     160535.176402  TM   14
[0008,0033]    ContentTime    112304    TM   6
[0008,0050]    AccessionNumber     3011926318851597    SH   16
[0008,0060]    Modality  CT   CS   2
[0008,0070]    Manufacturer        LO   0
[0008,0090]    ReferringPhysicianName        PN   0
[0008,1010]    StationName    CT54530   SH   8
[0008,1030]    StudyDescription         LO   0
[0008,103e]    SeriesDescription   FIDUCIALS  1.0  SPO  cor LO
     24
[0008,1090]    ManufacturerModelName         LO   0
[0010,0010]    PatientName         PN   0
[0010,0020]    PatientID TCGA-06-5410   LO   12
[0010,0030]    PatientBirthDate         DA   0
[0010,0040]    PatientSex     F    CS   2
[0010,1010]    PatientAge          AS   0
[0010,1030]    PatientWeight       DS   0
[0012,0062]    PatientIdentityRemoved   YES  CS   4
[0012,0063]    DeidentificationMethod
     DCM:113100/113105/113107/113108/113109/113111     LO   46
[0013,0010]    PrivateCreator CTP  LO   4
[0013,1010]    Unknown Tag & Data  54   UN   8
[0013,1013]    Unknown Tag & Data  34   UN   8
[0018,0015]    BodyPartExamined    BRAIN     CS   6
[0018,0050]    SliceThickness 1    DS   2
[0018,0060]    KVP  120  DS   4
[0018,0090]    DataCollectionDiameter   500  DS   4
[0018,1000]    DeviceSerialNumber  54530     LO   6
[0018,1020]    SoftwareVersions    syngo CT 2007S LO   14
[0018,1030]    ProtocolName   FIDUCIALS LO   10
[0018,1100]    ReconstructionDiameter   162  DS   4
[0018,1110]    DistanceSourceToDetector 1040 DS   4
```

```
[0018,1111]    DistanceSourceToPatient  570  DS   4
[0018,1120]    GantryDetectorTilt  0    DS   2
[0018,1130]    TableHeight    207  DS   4
[0018,1140]    RotationDirection   CW   CS   2
[0018,1150]    ExposureTime   1000 IS   4
[0018,1151]    XRayTubeCurrent     240  IS   4
[0018,1152]    Exposure  300  IS   4
[0018,1160]    FilterType     0    SH   2
[0018,1170]    GeneratorPower 28   IS   2
[0018,1190]    FocalSpots     1.2  DS   4
[0018,1200]    DateOfLastCalibration    20100110  DA   8
[0018,1201]    TimeOfLastCalibration    051322.000000  TM   14
[0018,1210]    ConvolutionKernel   H60s SH   4
[0018,5100]    PatientPosition     HFS  CS   4
[0020,000d]    StudyInstanceUID
     1.3.6.1.4.1.14519.5.2.1.4591.4001.303546620668041504180142477000     UI   64
[0020,000e]    SeriesInstanceUID
     1.3.6.1.4.1.14519.5.2.1.4591.4001.192263247216768060808003960215     UI   64
[0020,0010]    StudyID        SH   0
[0020,0011]    SeriesNumber   8    IS   2
[0020,0012]    AcquisitionNumber   3    IS   2
[0020,0013]    InstanceNumber 167  IS   4
[0020,0032]    ImagePositionPatient     [3] -78.548796875, -
113.951, -16.614203125   DS   36
[0020,0037]    ImageOrientationPatient  [6] 1, 0, 0, 0, 0, -1
     DS   12
[0020,0052]    FrameOfReferenceUID
     1.3.6.1.4.1.14519.5.2.1.4591.4001.229198106833719476153705175357     UI   64
[0020,1040]    PositionReferenceIndicator         LO   0
[0020,4000]    ImageComments  C- 1.0MM SAG SHARP  LT   18
[0028,0002]    SamplesPerPixel     1    US   2
[0028,0004]    PhotometricInterpretation     MONOCHROME2    CS
     12
[0028,0010]    Rows 512  US   2
[0028,0011]    Columns   512  US   2
[0028,0030]    PixelSpacing   [2] 0.31640625, 0.31640625    DS
     22
[0028,0100]    BitsAllocated  16   US   2
[0028,0101]    BitsStored     16   US   2
[0028,0102]    HighBit   15   US   2
[0028,0103]    PixelRepresentation 0    US   2
[0028,0106]    SmallestImagePixelValue  0    US   2
[0028,0107]    LargestImagePixelValue   2793 US   2
```

```
[0028,0303]    LongitudinalTemporalInformationModified MODIFIED
     SH   8
[0028,1050]    WindowCenter   1396.500000    DS   12
[0028,1051]    WindowWidth    2793.000000    DS   12
[0028,1052]    RescaleIntercept    00   DS   2
[0028,1053]    RescaleSlope   01   DS   2
[0028,1055]    WindowCenterWidthExplanation  [2] WINDOW1,
WINDOW2   LO   16
[0040,2016]    PlacerOrderNumberImagingServiceRequest       LO
     0
[0040,2017]    FillerOrderNumberImagingServiceRequest       LO
     0
[0040,a075]    VerifyingObserverName    Removed by CTP PN   14
[0040,a123]    PersonName     Removed by CTP PN   14
[0070,0084]    ContentCreatorName       PN   0
[7fe0,0010]    PixelData 0033 OW   524288
```

Appendix C -Poiseuille Inlet Flow code (Provided by Mrigank Dhingra - Virginia Tech, March 2024.)

```
#include "udf.h"
DEFINE_PROFILE(poiseuille_velocity, thread, position)
{
    face_t f;
    real x[ND_ND]; /* ND_ND is the number of dimensions */
    real r, velocity;
    begin_f_loop(f, thread)
    {
        F_CENTROID(x,f,thread); /* Get the centroid coordinates
of the face */
        /* Assuming the flow is along the y-axis and the pipe is
aligned with the z-axis */
        /* Calculate the radial distance from the center
(assuming center at y=0) */
        r = sqrt(x[0]*x[0] + x[2]*x[2]); /* x[0] and x[2]
correspond to x and z coordinates, respectively */
        /* Calculate the velocity based on Poiseuille's law */
        velocity = 0.01 * (1 - pow((r/0.03), 2));
        /* Set the velocity profile */
        F_PROFILE(f, thread, position) = velocity;
    }
    end_f_loop(f, thread)
}
```

Appendix D: ANSYS Project Schematic

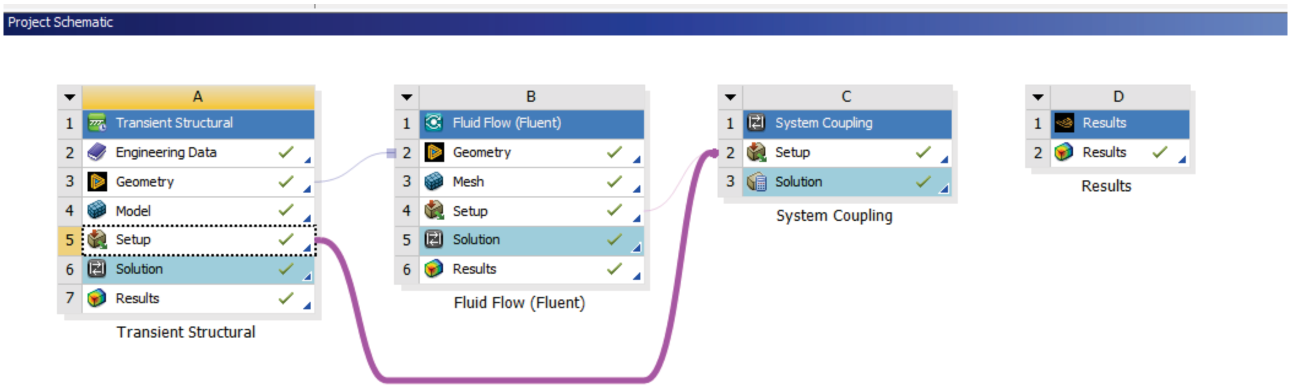

Figure A2

Appendix: E

Table A1: Data for Ogden Curve Fitting

Uniaxial Test Data	
Strain (mm mm^-1)	Stress (MPa)
0	0
0.011665	0.085112
0.022715	0.140359
0.033918	0.188141
0.045122	0.22796
0.055711	0.264045
0.066454	0.299633
0.077351	0.329993
0.088094	0.35936
0.09899	0.388228
0.109581	0.41411
0.120323	0.439494
0.131067	0.463882
0.141503	0.487276
0.1524	0.508678
0.162836	0.529831
0.173732	0.550736
0.184015	0.570895
0.194758	0.590305
0.205194	0.610214
0.215477	0.628381
0.225913	0.646549
0.236656	0.664467
0.247553	0.683132
0.25845	0.700552
0.268733	0.717724
0.279783	0.734895
0.290372	0.75356
0.300808	0.769488
0.311552	0.78641
0.322294	0.801591
0.333038	0.819509
0.343781	0.835188
0.354831	0.85211
0.365267	0.868287
0.376317	0.88496
0.386447	0.900888
0.39673	0.91781
0.407625	0.933738
0.418062	0.949914

0.428958	0.967085
0.439548	0.983013
0.449985	1.000433
0.460267	1.017853
0.471317	1.034279
0.4816	1.05145
0.492343	1.070115
0.502933	1.088531
0.51383	1.107195
0.523959	1.127851
0.534702	1.146267
0.544984	1.166674
0.555574	1.18708
0.56601	1.209728
0.576446	1.231379
0.587036	1.255269
0.597319	1.280156
0.607448	1.305541
0.617577	1.332915
0.628013	1.361784
0.638143	1.392891
0.648272	1.424994
0.658401	1.460831
0.66853	1.499653
0.67866	1.54196
Biaxial Test Data	
Strain (mm mm^-1)	Stress (MPa)
0	0
0.005654	0.12375
0.012419	0.200811
0.019286	0.263535
0.026454	0.320316
0.033725	0.371062
0.041096	0.416242
0.048164	0.456329
0.055535	0.494812
0.062805	0.531314
0.070277	0.565176
0.077547	0.597622
0.08512	0.628937
0.092491	0.657045
0.100064	0.686474
0.10784	0.715713
0.115412	0.740048

0.123188	0.764949
0.131265	0.790982
0.139444	0.814939
0.147522	0.838991
0.155802	0.863798
0.164283	0.88851
0.172664	0.911902
0.181348	0.936237
0.190032	0.959818
0.19922	0.982455
0.208308	1.007167
0.217497	1.029898
0.226685	1.053196
0.236176	1.077531
0.24587	1.103375
0.25516	1.128464
0.264955	1.154309
0.274849	1.176757
0.284745	1.205053
0.294842	1.230332
0.30494	1.258628
0.315138	1.289
0.325539	1.319277
0.335939	1.349461
0.346238	1.382473
0.356739	1.419541
0.367039	1.456516
0.377237	1.494621
0.387637	1.536689
0.397734	1.582812
0.408235	1.630539
0.418131	1.686283
0.428329	1.745705
0.438326	1.811947
Shear Test Data	
Strain (mm mm^-1)	Stress (MPa)
0	0
0.012065	0.139433
0.025226	0.227981
0.037657	0.297004
0.049905	0.356078
0.062427	0.408686
0.074493	0.456129
0.087472	0.498534

0.099993	0.54031
0.112424	0.577635
0.124398	0.613154
0.137102	0.646491
0.149899	0.678231
0.161964	0.708462
0.174486	0.736843
0.187099	0.76468
0.199804	0.791286
0.2126	0.816897
0.225214	0.841836
0.23801	0.866103
0.251172	0.889783
0.263329	0.912371
0.276399	0.935211
0.289286	0.957799
0.301808	0.979884
0.314787	1.001296
0.32731	1.022877
0.340563	1.044205
0.352902	1.065198
0.365973	1.086527
0.378952	1.108024
0.391748	1.129268
0.404727	1.150512
0.41798	1.172093
0.431051	1.193841
0.443481	1.213323
0.456095	1.237758
0.469074	1.261102
0.48187	1.284613
0.494667	1.308378
0.507646	1.333149
0.520716	1.359179
0.533695	1.38563
0.545943	1.413845
0.558465	1.443234
0.57181	1.47422
0.584606	1.507053
0.597768	1.542572
0.610564	1.58058
0.62336	1.62139
0.635608	1.665726
0.648314	1.714596

0.660926	1.769177

References

[1] E. A. M. Hackenberg, V. Sallinen, L. Handolin, and V. Koljonen, “Victims of Severe Intimate Partner Violence Are Left Without Advocacy Intervention in Primary Care Emergency Rooms: A Prospective Observational Study,” *J Interpers Violence*, vol. 36, no. 15–16, pp. 7832–7854, Aug. 2021, doi: 10.1177/0886260519837649.

[2] J. De Boos, “Review article: Non-fatal strangulation: Hidden injuries, hidden risks,” *Emergency Medicine Australasia*, vol. 31, no. 3, pp. 302–308, 2019, doi: 10.1111/1742-6723.13243.

[3] J. Payne-James, “Non-fatal strangulation,” in *Current Practice in Forensic Medicine*, John Wiley & Sons, Ltd, 2022, pp. 81–108. doi: 10.1002/9781119684107.ch5.

[4] K. Monahan, S. Bannon, and K. Dams-O’Connor, “Nonfatal Strangulation (NFS) and Intimate Partner Violence: a Brief Overview,” *J Fam Viol*, vol. 37, no. 1, pp. 75–86, Jan. 2022, doi: 10.1007/s10896-020-00208-7.

[5] A. Foley, “Strangulation: Know the Symptoms, Save a Life,” *Journal of Emergency Nursing*, vol. 41, no. 1, pp. 89–90, Jan. 2015, doi: 10.1016/j.jen.2014.10.013.

[6] N. Glass *et al.*, “Non-fatal Strangulation is an Important Risk Factor for Homicide of Women,” *The Journal of Emergency Medicine*, vol. 35, no. 3, pp. 329–335, Oct. 2008, doi: 10.1016/j.jemermed.2007.02.065.

[7] R. A. Sabo, W. C. Hanigan, K. Flessner, J. Rose, and M. Aaland, “Strangulation Injuries in Children. Part 1. Clinical Analysis,” *Journal of Trauma and Acute Care Surgery*, vol. 40, no. 1, p. 68, Jan. 1996.

[8] V. Yekhalov and natalia Khobotova, *New stages of development of modern science in Ukraine and EU countries*. Publishing House “Baltija Publishing,” 2019. doi: 10.30525/978-9934-588-15-0.

[9] A. J. Pritchard, A. Reckdenwald, and C. Nordham, “Nonfatal Strangulation as Part of Domestic Violence: A Review of Research,” *Trauma, Violence, & Abuse*, vol. 18, no. 4, pp. 407–424, Oct. 2017, doi: 10.1177/1524838015622439.

[10] A. Reckdenwald, C. Nordham, A. Pritchard, and B. Francis, “Identification of Nonfatal Strangulation by 911 Dispatchers: Suggestions for Advances Toward Evidence-Based Prosecution,” *Violence Vict*, vol. 32, no. 3, pp. 506–520, 2017, doi: 10.1891/0886-6708.VV-D-15-00157.

[11] Y. Bing, D. Garcia-Gonzalez, N. Voets, and A. Jérusalem, “Medical imaging based in silico head model for ischaemic stroke simulation,” *Journal of the Mechanical Behavior of Biomedical Materials*, vol. 101, p. 103442, Jan. 2020, doi: 10.1016/j.jmbbm.2019.103442.

[12] K. Jain, J. Jiang, C. Strother, and K.-A. Mardal, “Transitional hemodynamics in intracranial aneurysms — Comparative velocity investigations with high resolution lattice Boltzmann simulations, normal resolution ANSYS simulations, and MR imaging,” *Medical Physics*, vol. 43, no. 11, pp. 6186–6198, 2016, doi: 10.1118/1.4964793.

[13] Z. Li and C. Kleinstreuer, “Blood flow and structure interactions in a stented abdominal aortic aneurysm model,” *Medical Engineering & Physics*, vol. 27, no. 5, pp. 369–382, Jun. 2005, doi: 10.1016/j.medengphy.2004.12.003.

[14] “File Pack for 3D Printing with Osirix Tutorial,” embodi3D.com. Accessed: Aug. 21, 2024. [Online]. Available: https://www.embodi3d.com/files/file/115-file-pack-for-3d-printing-with-osirix-tutorial/

[15] S. Eisová, P. Velemínský, J. Velemínská, and E. Bruner, “Diploic vein morphology in normal and craniosynostotic adult human skulls,” *Journal of Morphology*, vol. 283, no. 10, pp. 1318–1336, 2022, doi: 10.1002/jmor.21505.

[16] I. Hershkovitz *et al.*, “The elusive diploic veins: Anthropological and anatomical perspective,” *American Journal of Physical Anthropology*, vol. 108, no. 3, pp. 345–358, 1999, doi: 10.1002/(SICI)1096-8644(199903)108:3<345::AID-AJPA9>3.0.CO;2-S.

[17] “Skull | Definition, Anatomy, & Function,” Encyclopedia Britannica. Accessed: Jul. 23, 2024. [Online]. Available: https://www.britannica.com/science/skull

[18] S. Lachkar, M.-M. Dols, B. Ishak, J. Iwanaga, and R. S. Tubbs, “The Diploic Veins: A Comprehensive Review with Clinical Applications,” *Cureus*, vol. 11, no. 4, p. e4422, doi: 10.7759/cureus.4422.

[19] R. S. Tubbs, E. G. Salter, J. C. I. Wellons, J. P. Blount, and W. J. Oakes, “THE SPHENOPARIETAL SINUS,” *Operative Neurosurgery*, vol. 60, no. 2, p. 9, Feb. 2007, doi: 10.1227/01.NEU.0000249241.35731.C6.

[20] M. J. Lohr, G. P. Sugerman, S. Kakaletsis, E. Lejeune, and M. K. Rausch, “An introduction to the Ogden model in biomechanics: benefits, implementation tools and limitations,” *Philosophical Transactions of the Royal Society A: Mathematical, Physical and Engineering Sciences*, vol. 380, no. 2234, p. 20210365, Aug. 2022, doi: 10.1098/rsta.2021.0365.

[21] C. Paz, E. Suárez, A. Cabarcos, and S. I. S. Pinto, “Numerical Study of a Thrombus Migration Risk in Aneurysm After Coil Embolization in Patient Cases: FSI Modelling,” *Cardiovasc Eng Tech*, vol. 14, no. 4, pp. 544–559, Aug. 2023, doi: 10.1007/s13239-023-00672-4.

[22] M. Rackl, “Curve Fitting for Ogden, Yeoh and Polynomial Models”.

[23] “How to Perform Curve-fitting for Hyperelastic Material Models — Lesson 1,” ANSYS Innovation Courses. Accessed: Aug. 19, 2024. [Online]. Available: https://innovationspace.ansys.com/courses/courses/topics-in-hyperelasticity-using-ansys-mechanical/lessons/how-to-perform-curve-fitting-for-hyperelastic-material-models-lesson-1/

[24] S. Hodis and M. Zamir, “Mechanical events within the arterial wall under the forces of pulsatile flow: A review,” *Journal of the Mechanical Behavior of Biomedical Materials*, vol. 4, no. 8, pp. 1595–1602, Nov. 2011, doi: 10.1016/j.jmbbm.2011.01.005.

[25] N. Westerhof, N. Stergiopulos, and M. I. M. Noble, “Law of Poiseuille,” in *Snapshots of Hemodynamics: An Aid for Clinical Research and Graduate Education*, N. Westerhof, N. Stergiopulos, and M. I. M. Noble, Eds., Boston, MA: Springer US, 2010, pp. 9–14. doi: 10.1007/978-1-4419-6363-5_2.

[26] K. B. Chandran, “Biofluid Mechanics”.

[27] “Introduction To ANSYS Fluent: A Beginner’s Guide - MR CFD.” Accessed: Jul. 18, 2024. [Online]. Available: https://www.mr-cfd.com/introduction-to-ansys-fluent-a-beginners-guide/

[28] E. J. Neuberger, R. Abdul Wahab, A. Jayakumar, B. J. Pfister, and V. Santhakumar, “Distinct effect of impact rise times on immediate and early neuropathology after brain injury in juvenile rats,” *J of Neuroscience Research*, vol. 92, no. 10, pp. 1350–1361, Oct. 2014, doi: 10.1002/jnr.23401.

[29] O. O. Adigun and M. A. Al-Dhahir, “Anatomy, Head and Neck: Cerebrospinal Fluid,” in *StatPearls*, Treasure Island (FL): StatPearls Publishing, 2024. Accessed: Apr. 18, 2024. [Online]. Available: http://www.ncbi.nlm.nih.gov/books/NBK459286/

[30] S. K. Chimakurthi, S. Reuss, M. Tooley, and S. Scampoli, “ANSYS Workbench System Coupling: a state-of-the-art computational framework for analyzing multiphysics problems,” *Engineering with Computers*, vol. 34, no. 2, pp. 385–411, Apr. 2018, doi: 10.1007/s00366-017-0548-4.

[31] “What is Equivalent Stress? | Ansys.” Accessed: Jul. 03, 2024. [Online]. Available: https://www.ansys.com/blog/what-is-equivalent-stress

[32] B. Kaur, P. Kaur, and A. K. Jain, “Analysis of deformation of RC beam with addition of fly ash: a Finite element based modeling,” vol. 07, no. 05, 2020.

[33] “Static Pressure Vs.Dynamic Pressure Vs.Total Pressure in Fluids.” Accessed: Jul. 24, 2024. [Online]. Available: https://sino-inst.com/fluid-pressure-static-pressure-vs-dynamic-pressure-vs-total-pressure/

[34] “Bernoulli’s Principle states that as the speed of a moving fluid increases, the pressure within the fluid decreases”.

[35] “What Is The Relation Between Pressure And Velocity? - BYJU’S,” BYJUS. Accessed: Jul. 25, 2024. [Online]. Available: https://byjus.com/physics/relation-between-pressure-and-velocity/

[36] R. H. Riffenburgh, “Modeling Concepts and Methods,” in *Statistics in Medicine*, Elsevier, 2012, pp. 393–414. doi: 10.1016/B978-0-12-384864-2.00019-6.

[37] K. L. Monson, W. Goldsmith, N. M. Barbaro, and G. T. Manley, “Axial Mechanical Properties of Fresh Human Cerebral Blood Vessels,” *Journal of Biomechanical Engineering*, vol. 125, no. 2, pp. 288–294, Apr. 2003, doi: 10.1115/1.1554412.